

Growth of bilayer stanene on a magnetic topological insulator aided by a buffer layer

Sajal Barman^{1,†}, Pramod Bhakuni^{1,†}, Shuvam Sarkar¹, Joydipto Bhattacharya^{2,3},
Mohammad Balal¹, Mrinal Manna¹, Soumen Giri¹, Arnab Kumar Pariari⁴, Tomáš Skála⁵,
Markus Hückler⁴, Rajib Batabyal¹, Aparna Chakrabarti^{2,3}, and Sudipta Roy Barman^{1,*}

¹*UGC-DAE Consortium for Scientific Research,
Khandwa Road, Indore, 452001, India*

²*Theory and Simulations Laboratory, Raja Ramanna Centre for Advanced Technology,
Indore 452013, Madhya Pradesh, India*

³*Homi Bhabha National Institute, Training School Complex,
Anushakti Nagar, Mumbai 400094, Maharashtra, India*

⁴*Department of Condensed Matter Physics,
Weizmann Institute of Science, Rehovot, Israel*

⁵*Charles University, Faculty of Mathematics and Physics,
V Holešovičkách 2, CZ-18000 Prague 8, Czech Republic.*

[†]*Both authors contributed equally.*

Abstract

Stanene, a two-dimensional counterpart to graphene, has the potential to exhibit novel quantum phenomena when grown on a magnetic topological insulator (MTI). This work demonstrates the formation of up to bilayer stanene on 30% Sb-doped MnBi_2Te_4 (MBST), a well known MTI, albeit with a buffer layer (BL) in between. Angle-resolved photoemission spectroscopy (ARPES), when combined with density functional theory (DFT), reveals stanene related bands such as two hole-like bands and an inverted parabolic band around the $\bar{\Gamma}$ point. An outer hole-like band traverses the Fermi level (E_F) and gives rise to a hexagonal Fermi surface, showing that stanene on MBST is metallic. In contrast, a bandgap of 0.8 eV is observed at the \bar{K} point. We find that DFT shows good agreement with ARPES only when the BL and hydrogen passivation of the top Sn layer are considered in the calculation. Scanning tunneling microscopy (STM) establishes the honeycomb buckled structure of stanene. A stanene-related component is also detected in the Sn d core level spectra, in addition to a BL-related component. The BL, which forms because of the chemical bonding between Sn and the top two layers of MBST, has an ordered crystal lattice with random anti-site defects. The composition of the BL is estimated to be Sn:Te:Bi/Sb \approx 2:1:1 from x-ray photoelectron spectroscopy. Low energy electron diffraction shows that the lattice constant of stanene is marginally larger than that of MBST, and the STM result aligns with this. The BL bridges this disparity and provides a platform for stanene growth.

I. INTRODUCTION

Stanene is a two dimensional (2D) topological insulator (TI) or quantum spin Hall (QSH) phase characterized by the topologically protected helical boundary states that are immune to backscattering [1–3]. It exhibits a honeycomb structure, similar to graphene [4, 5]. The first experimental realization of monolayer stanene was reported on a TI, namely, bismuth telluride (Bi_2Te_3) [6]. A later study on Cu(111) reported the growth of ultra-flat stanene with a band inversion [7]. The recent discovery of superconductivity in few-layer stanene grown on Bi [8] and PbTe/ Bi_2Te_3 [9, 10] has revitalized this area of research. Superconductivity along with the QSH state might give rise to an interesting possibility of realizing proximity-induced topological superconductivity [11–14]. Liao *et al.* [9] reported that the superconducting transition temperature (T_C) could be increased from 0.5 K to 1.2 K by enhancing the thickness of the PbTe buffer layer (BL). Buffer layers such as Pd_2Sn and Ag_2Sn were reported for stanene that was grown on Pd(111) [15] and Ag(111) [16],

respectively. BL formation has also played a constructive role in 2D systems, such as for achieving quasi-free-standing bilayer graphene on SiC [17, 18] and silicene on Ag [19].

Tellurides have been at the forefront of materials research, such as the discovery of the TI phase in Bi_2Te_3 [20, 21]; high thermoelectric performance in BiSbTe [22]; a new topological phase Kramers nodal line in rare earth chalcogenide LaTe_3 [23]; large magnetoresistance, vortices in electron flow, superconductivity, and higher order topology in transition metal dichalcogenides [24–27]; and the intrinsic magnetic topological insulator (MTI) phase in MnBi_2Te_4 (MBT) [28–31], to mention a few. MBT is a layered material with the (0001) surface being Te terminated, Te forms the top layer of a Te-Bi-Te-Mn-Te-Bi-Te “septuple”, where multiple septuple layers are coupled by van der Waals interaction. MBT hosts the topological surface state located within the energy gap between the bulk valence and the conduction band stemming from the topologically nontrivial bulk bands [28, 32]. However, because of n-type doping intrinsically present in MBT, these bands are shifted to higher binding energy such that the Dirac point appears ~ 0.28 eV below the Fermi level (E_F) [28, 32, 33]. It was shown that substitution of Bi by Sb in MBT shifts back the bands towards E_F such that the topological surface states cross E_F [34–36].

Stanene is a member of the X-ene family [1, 2, 37, 38] and has great promise for application in spintronics [39], nanoelectronics [40], catalysis [41], and biomedicine [42]. Deposition of Sn on chalcogenides and related substrates has produced stanene [6–10, 15, 16, 43–46] as well as surface alloys of Sn [47–49] with interesting properties. Therefore, although stanene has previously been grown on non-magnetic topological and non-topological substrates, the impact of a magnetic topological substrate like MBT or Sb-doped MBT on its properties may be intriguing, given that the quantum anomalous Hall effect can result from magnetic interaction with the QSH state [2, 50–53]. Furthermore, proximity-induced superconductivity might appear in an MTI due to a two-dimensional superconducting stanene grown on it, which might facilitate the existence of Majorana fermions and find applications in the field of quantum computing. While no such work exists in the literature to date, a study of stanene on Bi_2Te_3 [6] – structurally similar to MBT with a Te-terminated “quintuple” layer (Te-Bi-Te-Bi-Te) – suggested weak-coupling between stanene and the substrate with no chemical bonding. In contrast, a relatively recent research [44] has provided evidence of a BL formed by an interfacial chemical reaction of Sn with Bi_2Te_3 .

Based on our initial investigations, it appears that both Sb-doped MBT and MBT, which have similar structure, termination, and lattice constants, have the ability to promote the growth of stanene. However, for this study, we have chosen to focus on conducting a thorough analysis of the

former to examine the effect of Sn deposition on the bulk bands that disperse up to the E_F . Combining multiple techniques such as angle resolved photoemission spectroscopy (ARPES), scanning tunneling microscopy (STM), density functional theory (DFT), x-ray photoelectron spectroscopy (XPS), and low energy electron diffraction (LEED), we demonstrate the formation of monolayer and bilayer stanene on $\sim 30\%$ Sb-doped MnBi_2Te_4 (henceforth referred to as MBST) at room temperature. This is the first report of stanene growth, or any X-ene growth, on an MTI. Height profile analysis of atomic resolution STM topography images further establishes stanene formation, which is preceded by the growth of a BL. The XPS analysis reveals that the BL forms through chemical bonding between Sn and the two uppermost layers of MBST. It has a thickness of 0.9 nm and a composition ratio of $\approx 2:1:1$ (Sn:Te:Bi/Sb). ARPES shows two hole-like and an inverted parabolic stanene bands around the $\bar{\Gamma}$ point. An outer hole-like band crosses the Fermi level (E_F) creating a hexagonal Fermi surface, but a bandgap is seen at the \bar{K} point. DFT calculation that includes the BL and hydrogen passivation of the top stanene layer exhibits good agreement with ARPES.

II. METHODS

Photoemission spectroscopy: The ARPES and XPS measurements were performed using a helium discharge lamp equipped with a monochromator and a monochromatized Al $K\alpha$ source, respectively that are mounted on an analysis chamber with a base pressure of 1×10^{-10} mbar. The photoelectrons were detected using the R4000 hemispherical electron energy analyzer from Scienta Omicron GmbH with the energy resolution set at better than 15 meV, while the angular resolution was 1° . The analyzer is equipped with a wide angle lens that has an acceptance angle of $\pm 15^\circ$. The XPS measurements were performed using the transmission lens mode of the analyzer with an energy resolution of 0.33 eV. The LEED equipment comprised of a four-grid rear-view optics system. Core level spectroscopy (CLS) using low energy photons (90 eV) was performed using synchrotron radiation at the Materials Science Beamline at Elettra in Trieste, Italy. Hard x-ray photoelectron spectroscopy (HAXPES) using 6 keV photon energy was performed at the P22 beamline in PETRA III of Deutsches Elektronen-Synchrotron in Hamburg, Germany.

The analysis of the photoemission data was performed using Igor Pro, ver 9 from Wavemetrics Inc. The core level spectra were fitted with the least square error minimization method as in our earlier works [54] with the instrumental resolution represented by a Gaussian function of fixed

width. The energy position, intensity, life-time broadening, and the Tougaard background [55] parameter were varied during the fitting. The position of the bands has been determined from the raw ARPES intensity plot by taking cuts along the momentum axis at a fixed energy to obtain the momentum distribution curves (MDCs). The energy distribution curves (EDCs) are obtained from cuts along the energy axis at a fixed momentum. The band positions are identified by least-squares curve fitting of the peaks of the cuts with Lorentzian functions and a linear background. The second derivative analysis of the raw ARPES intensity plots has been performed with respect to the energy axis to show the bands with better contrast, as in our earlier work [49].

STM: The STM measurements were performed using a variable temperature STM from Scienta Omicron GmbH at a base pressure of 4×10^{-11} mbar. Electrochemically etched polycrystalline W tips as well as mechanically grinded Pt-Ir tips were used. These tips were cleaned *in-situ* using Ar^+ ion sputtering and applying voltage pulses. The tip was biased and the sample was kept at the ground potential. The average height of each layer is calculated by averaging over more than 50 height profiles and also by height histogram. The STM images were analyzed using the SPIP and Gwyddion software [56]. Atomic resolution STM images are enhanced using Fourier filtering.

Density functional theory: The DFT based first-principles calculations were performed using the projector-augmented-wave (PAW) [57] potential and the exchange correlation functional Perdew–Burke–Ernzerhof (PBE) generalized gradient approximation (GGA) [58], as implemented in the Vienna ab initio simulation package (VASP) [59]. Periodic slab calculations have been performed with a vacuum of 1.5 nm along the z direction to overcome the interactions between the periodic images. The slab calculations were performed with a plane wave basis with an energy cut-off of 400 eV, a $13 \times 13 \times 1$ Monkhorst-Pack k grid [60] was used for the k -space sampling. A force convergence criterion of $0.01 \text{ eV } \text{\AA}^{-1}$ was selected for structural optimization. The spin–orbit coupling (SOC) interaction was included in the electronic structure calculation. The band structure calculations were performed along the high-symmetry path \bar{M} (0.5, 0.0, 0.0) – $\bar{\Gamma}$ (0.0, 0.0, 0.0) – \bar{K} (1/3, 1/3, 0.0). The VESTA program [61] has been employed for the representation and visualization of the crystal structures. The orbital character of the bands is obtained by projecting the Bloch wave function on the orbitals.

Sample preparation and characterization: Stanene was grown by deposition of Sn (99.99%) using a water-cooled Knudsen cell [62] equipped with a mechanical shutter at an operating temperature

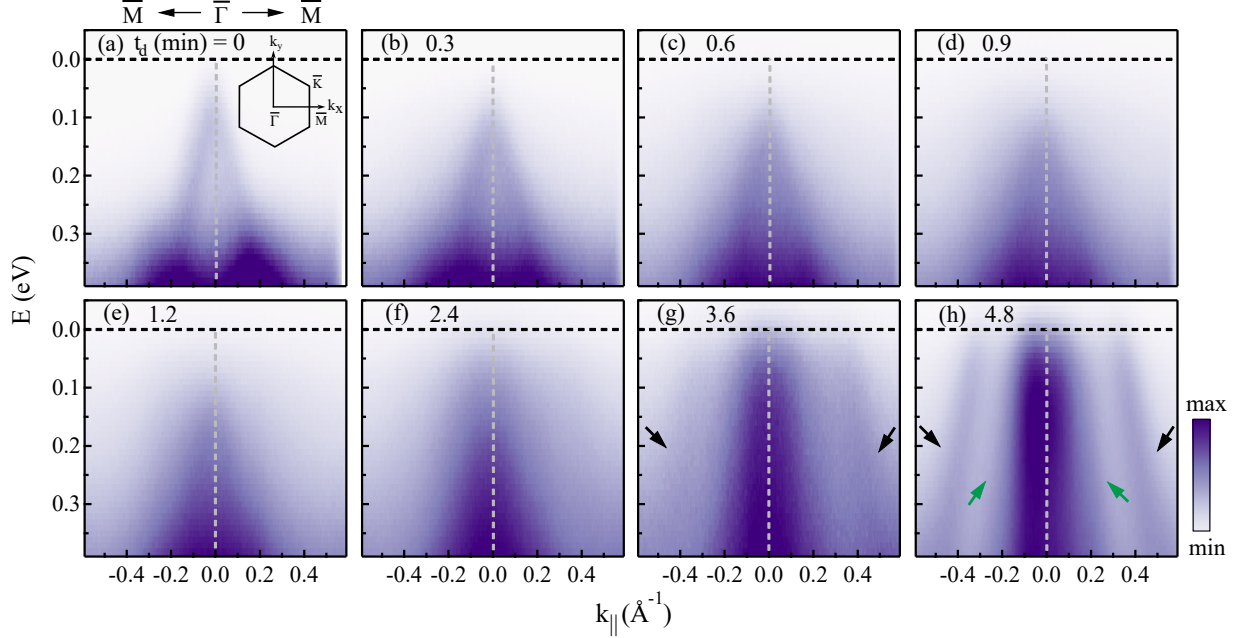


Figure 1. (a-h) ARPES intensity plots as a function of Sn deposition on MBST, where the binding energy (E) in the vertical axis is plotted against the momentum parallel to the surface ($k_{||}$) in the horizontal axis from $\bar{\Gamma}$ towards \bar{M} with increasing deposition time (t_d), as mentioned in unit of min at the top of each panel. The black (green) arrows show the outer (inner) band related to stanene. The Brillouin zone (BZ) is shown in the inset of panel **a**. The zero of E corresponds to the E_F .

of 1073 K and chamber pressure of 2×10^{-10} mbar. The substrate temperature was 303-313 K and its distance from the Knudsen cell was ~ 70 mm and the angle of deposition was $\sim 45^\circ$.

In-situ peeling with a scotch tape exposed an atomically clean (0001) surface of the substrate MBST crystal. The peeling was performed at room temperature in the preparation chamber at a pressure of 1×10^{-10} mbar. The MBST single crystal was grown by the flux method following a similar temperature profile described in previous reports [35, 63]. In order to grow $n\%$ Sb-doped MBST crystal, a mixture of high purity ($\geq 99.999\%$) Mn powder, Bi shots, Te chunks, and Sb shots in a molar ratio Mn: Sb: Bi: Te = 1: $10 \times n$: $10 \times (1 - n)$: 16 were placed in an alumina crucible of a Canfield crucible set. Then, the entire crucible set was sealed in an evacuated silica ampule at $< 10^{-5}$ mbar pressure. The sealed ampule was heated to 1173 K for two days and kept at that

temperature for 12 hours followed by a slow cooling 10 K/hr down to 878 K. At the final stage of the temperature profile, the ampule was cooled from 878 K to 863 K in 336 hrs and kept at that temperature for 72 hrs followed by centrifuge at 3000 rpm to remove the excess flux from crystals. Plate-like shiny crystals are obtained from the bottom crucible.

The amount of Sb doping in our MBST crystal has been experimentally determined from the Sb $4d$ and Bi $5d$ peaks measured by HAXPES. It is an appropriate method for obtaining information about the bulk electronic states [64]. This is because of the large inelastic mean free path (IMFP) of the photoelectrons, which in the case of MBST is estimated to be about 9 nm [65]. From the intensities of the Sb $4d$ and Bi $5d$ peaks shown in Fig. S1 of the supplementary material (SM) [66] obtained from multi parameter core level fitting and considering the respective photoemission cross sections [67], we find the Sb doping to be $\sim 30\%$. Also, earlier research [34, 36] has shown that the Sb doping level influences the position of the valence and conduction bands of MBST. It is clear that our crystal has 30% Sb level because our ARPES intensity plot in Fig. 1(a) is similar to Fig. 2(e) of Ref. 34 and Fig. 2(d) of Ref. 36, both of which also have a 30% Sb doping. Furthermore, the magnetization (M) versus temperature at a magnetic field (H) of 0.1 Tesla shows the Neel temperature to be 24 K, whereas $M(H)$ measurement at 2 K shows the spin flop transition from antiferromagnetic to canted antiferromagnetic at 2.3 Tesla (Fig. S2 of the SM [66]), in agreement with literature [34, 63]. The unit cell of MBST is shown in Fig. S3(a) of the SM [66]. The MBST crystals with dimensions of 4-5 mm that have been used in this work are shown in Fig. S3(b) of the SM [66].

III. RESULTS AND DISCUSSION

A. ARPES study of sequential Sn depositions on MBST

Figure 1(a) shows an inverted “V”-like valence band of MBST with its maximum close to E_F at the $\bar{\Gamma}$ point, as has been reported in literature [34–36, 68]. It disperses from the maximum down to about 0.3 eV binding energy (E) at 0.2 \AA^{-1} . The substitution of Bi by Sb induces p-type doping in MBST [34] causing the band maximum to appear close to E_F in contrast to MBT, where it is observed ~ 0.4 eV below E_F due to the inherent n-type doping [32].

An intriguing observation with Sn deposition is a gradual, rigid band-like shift of the MBST bulk valence band maximum towards larger E , as shown in Figs. 1(b) to 1(e) measured towards the

$\bar{\Gamma}$ - \bar{M} direction (see Fig. S4 of SM [66] for the second derivative intensity plots). A quantitative estimate of this shift is about 65 meV for a deposition time (t_d) of 1.2 min, which is obtained by fitting the energy distribution curves (EDCs) drawn at $k_{\parallel}=0$ with Lorentzian functions (Fig. S5 of the SM [66]). The ARPES intensity plots towards the $\bar{\Gamma}$ - \bar{K} direction also show a similar shift of the band maximum; see Fig. S6 and S7 of the SM [66] for the raw and second derivative images, respectively. The observed shift contrasts with the effect of p-type doping by Sb and indicates that Sn deposition results in n-type doping. This implies the formation of a chemical bond between Sn and the substrate due to charge transfer. Note that Figs. 1(b) to 1(e) show that the shift is gradual with t_d , while, on the other hand, a discontinuous shift is expected across an intrinsic bulk band gap (0.2 eV for MBST). So, the observed gradual shift suggests the presence of the in-gap topological surface states [34, 35], but these states are not observed directly in our ARPES data recorded with 21.2 eV He I radiation due to the photoemission matrix element effect [32].

For the largest deposition of $t_d=4.8$ min, the ARPES intensity plot shows emergence of new bands [Fig. 1(h)]. An outer hole-like band indicated by black arrows is observed to disperse from close to E_F at about 0.36 \AA^{-1} to 0.4 eV at 0.5 \AA^{-1} . In addition, a weak inner hole-like band – highlighted by green arrows – is also visible. At a relatively smaller Sn deposition of $t_d=3.6$ min in Fig. 1(g), the outer band is also visible (black arrows). The ARPES bands and the Fermi surface for monolayer stanene are discussed in section III.E. Results of our DFT calculation are presented in section III.F and compared with ARPES. Prior to that in the next sections, we present the evidence of stanene and the BL formation from XPS, STM and LEED in sections III.B, III.C, and III.D, respectively.

B. Signature of stanene and buffer layer from core level spectroscopy

The growth mechanism of Sn on MBST has been determined by studying the core level spectra of Sn and the components of the substrate as a function of t_d . The discussion begins below with the Sn $3d_{5/2}$ spectra.

BL formation from Sn $3d_{5/2}$: Figure 2(a) shows that for $t_d \leq 2.4$ min, the spectra are well fitted with only one component, Sn_B (green curve). Sn_B appears at 485.3 eV [Fig. 2(b)] that is significantly shifted to a larger E from bulk Sn metal (484.7 eV). Rather, E of Sn_B is close to SnTe (485.4 eV [44, 69]) indicating that the Sn atoms react with the top Te layer of the (0001) surface

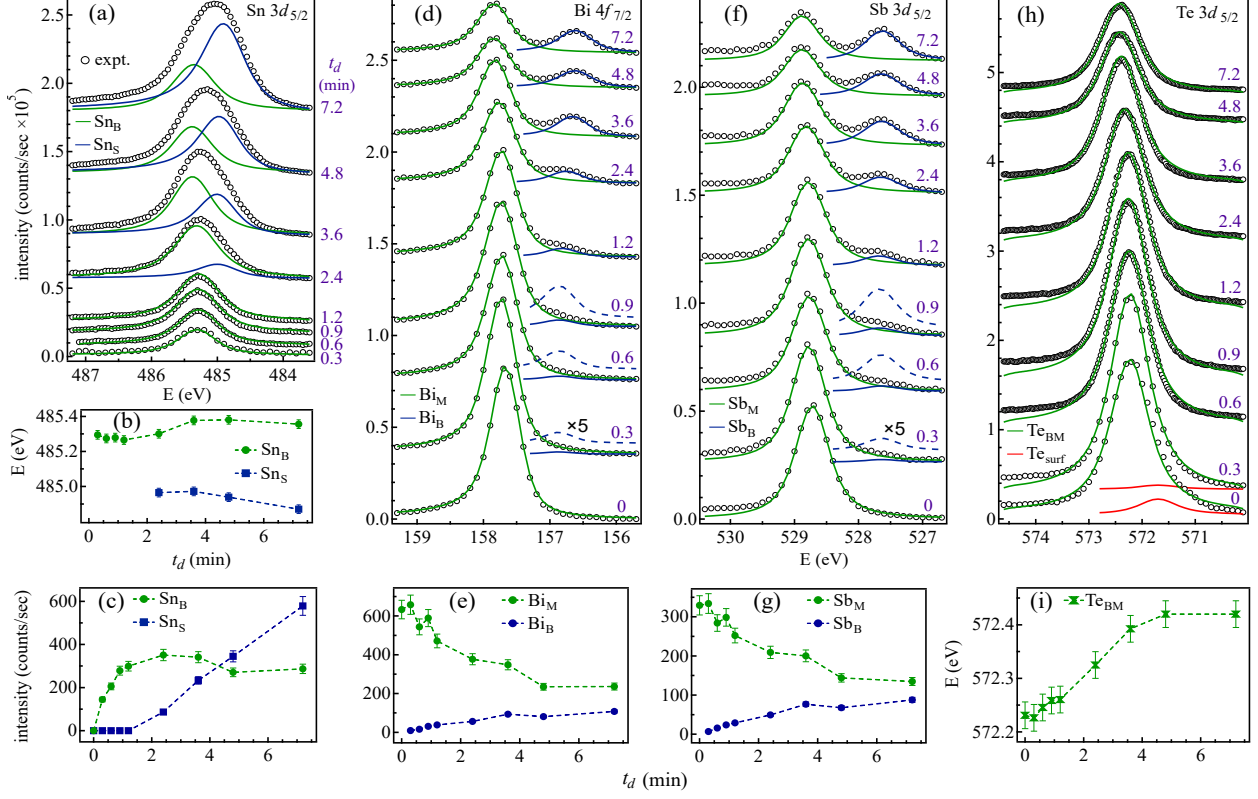


Figure 2. (a) Sn $3d_{5/2}$ core level spectra with two fitted components Sn_B and Sn_S for different t_d , as labeled in purple color on the right. (b) Binding energy (E) and (c) intensity of the components as a function of t_d . (d) Bi $4f_{7/2}$ and (f) Sb $3d_{5/2}$ core level spectra with two fitted components (blue and green curves). Intensity as a function of t_d for (e) Bi_M and Bi_B and (g) Sb_M and Sb_B components. (h) Te $3d_{5/2}$ core level spectra with the fitted components Te_{BM} and Te_{surf} , the latter becomes zero for $t_d \geq 0.6$ min; (i) $E(t_d)$ for Te_{BM} . The spectra in panels **a**, **d**, **f**, **h** are staggered vertically.

of MBST (Fig. S3(a) of the SM [66]) forming Sn-Te bonds by transferring electrons, which is also supported by ARPES [Figs. 1(b) to 1(e)]. This is also consistent with the smaller tendency of Sn to gain electrons because the electronegativity of Sn is 1.96 in the Pauling scale compared to Te with electronegativity of 2.1 [70]. The reaction between Sn and Te contributes to the formation of a BL. Interaction of Sn with Bi/Sb also contributes to the BL formation, as shown by the Bi $4f_{7/2}$ and Sb $3d_{5/2}$ core level spectra discussed below. The BL related component, Sn_B , is visible right from the beginning at $t_d = 0.3$ min and increases rapidly in intensity up to $t_d = 2.4$ min as the BL grows, but stagnates thereafter [Fig. 2(c)]. As discussed later in section III.C, a STM topography image [Fig. 3(c)] shows that the BL is almost fully formed and covers more than 90% of the surface at $t_d = 2.4$ min.

Evidence of Stanene from Sn $3d_{5/2}$: For $t_d \geq 2.4$ min, Sn $3d_{5/2}$ in Fig. 2(a) starts to show an extra component, Sn_S (blue curve), which is identified from our least square fitting. The details of the fitting are shown in Fig. S8 of the SM [66], where the components, background, and residual of the fitting are shown. Table S I enlists the values of the converged fitting parameters.

The Sn_S component of Sn $3d_{5/2}$ is related to stanene because it is observed only for $t_d \geq 2.4$ min, i.e., after BL formation is completed [Fig. 3(c)] and stanene related bands are visible in ARPES (Fig. 1, discussed further in sections III.E and III.F). It has zero intensity for $t_d \leq 1.2$ min [Fig. 2(c)], where neither ARPES nor STM [Fig. 3(a)] detect the stanene signature. Sn_S appears at $E = 484.95$ eV and becomes more intense than Sn_B at $t_d = 4.8$ min, where the stanene bands are unambiguously identified from ARPES [Fig. 1(h)].

Evidence of BL from Bi $4f_{7/2}$ and Sb $3d_{5/2}$: The analysis of the Bi $4f_{7/2}$ and Sb $3d_{5/2}$ core level spectra in Figs. 2(d) and 2(f), respectively, provide additional insight into the BL, where both Bi and Sb (referred to together as “Bi/Sb”) show a component (Bi/Sb)_B (blue curve, BL component) in addition to the main peak, (Bi/Sb)_M (green curve, bulk component from deeper layers). See also Figs. S9 and S10 and Tables S II and S III of the SM [66] for the details of the fitting. Bi_B and Sb_B appear at 156.85 eV and 527.65 eV, which are shifted by 0.85 and 1.15 eV, respectively, towards lower E compared to their respective main peaks. The significant shift in (Bi/Sb)_B suggests chemical bonding between Sn and Bi/Sb from the beginning, i.e., $t_d = 0.3$ min. E 's of (Bi/Sb)_B are smaller compared even to their corresponding elemental bulk values (156.9 and 528.2 for Bi and Sb, respectively [69]). This points to a bonding with Sn that would transfer electrons to Bi/Sb due to the larger electronegativity of Bi/Sb (2.02/2.05 [70]) compared to Sn (1.96). The (Bi/Sb)_B component has finite intensity from the outset ($t_d = 0.3$ min) [see the five times magnified blue dashed curves in Figs. 2(d) and 2(f) and the intensity variation in Figs. 2(e) and 2(g)] indicating the formation of Sn-Bi/Sb bonds, although Bi/Sb is below the Te layer (Fig. S3(a) of the SM [66]).

Te $3d_{5/2}$ and Mn $2p$ spectra : In Figs. 2(h) and 2(i), the effect of Sn-Te bonding on the Te $3d_{5/2}$ core level spectra is manifested by a shift towards larger E with respect to bare MBST. The spectra can be fitted with a single component denoted as Te_{BM} comprising of (i) Te_B i.e., the Te $3d_{5/2}$ signal from the BL that reacts with Sn forming Sn-Te like bonds, and (ii) Te_M i.e., the Te $3d_{5/2}$ signal from the deeper Te layers that do not react with Sn (see Fig. S11 and Table S IV of the SM [66] for details of fitting). Te_M and Te_B are not resolved as separate peaks within our resolution. This

is because the E of Te_M is 572.2 eV [determined from the bottom spectrum i.e., that of MBST in Fig. 2(h)], which is close to that of Te_B (~ 572.3 eV [69], which is the E of $\text{Te } 3d_{5/2}$ in SnTe).

Note that a surface core level peak, Te_{surf} , is observed for MBST ($t_d = 0$) that is shifted by 0.5 eV towards lower E from the main peak [red curves in Fig. 2(h)]. In Fig. S12 of the SM [66], it is confirmed by a difference spectrum between $t_d = 0$ min and 0.3 min, where it is suppressed in the latter due to a change in the surface potential caused by Sn deposition. Such surface core level peak – reported in other Te terminated surfaces [71, 72]– are generally related to a reduction in the coordination number of the surface Te atoms.

The Mn $2p$ spectrum of MBST [32] is hardly influenced by Sn deposition (Fig. S13 of the SM [66]). This observation indicates that the Mn layer, which is the fourth layer of the septuple, has minimal interaction with Sn and is unlikely to play a role in the formation of the BL.

Composition of the BL from XPS: The composition of the BL has been determined from the areas of the Sn_B , Te_B , Bi_B , and Sb_B components after dividing by their respective photoemission cross sections [67] and the analyzer transmission function. Since $\text{Te } 3d_{5/2}$ does not show a distinguishable BL component, Te_B has been extracted from the total Te signal, Te_{BM} , by calculating the contribution of the top or first Te layer that is involved in the BL formation using the equation $I_i = I_1 e^{-d_i/\lambda_i}$. Here, I_i = intensity of the i^{th} Te layer, I_1 = intensity of the top layer, d_i = depth of the i^{th} Te layer from the top surface, and λ_i is the inelastic mean free path [65] calculated by weighted averaging for the atoms in the region through which the electrons emitted from the i^{th} Te layer passes to reach the surface. The composition of the BL turns out to be 54% Sn, 23% Te, 13% Bi, and 10% Sb after averaging for $t_d \geq 2.4$ min i.e., after it is fully formed. Therefore, the ratio of Sn:Te:Bi/Sb atoms in the BL is $\approx 2:1:1$, which shows that it comprises of Sn atoms that bond with a nearly equal number of Te and Bi/Sb atoms. This is facilitated by the presence of random anti-site defects in the BL, as shown by our LEED study (section III.D).

Sn 4d and Bi 5d core level spectra: The Sn $4d_{3/2}$ and $4d_{5/2}$ peaks are observed at 25.5 and 24.40 eV as Sn deposition commences (Fig. S14 of the SM [66]). This is the BL related Sn_B component that is observed in Sn $3d_{5/2}$ spectra discussed above. A black dashed line shows that the Sn $4d_{3/2}$ intensity increases with position nearly unchanged up to $t_d = 1.1$ -1.2 min. However, at $t_d = 2.4$ -2.6 min, there is a small shift of ~ 0.09 eV to lower E with a change in shape, indicating appearance of a second component. This component becomes more intense compared to Sn_B for $t_d > 4.5$ min

and appears at $E = 25.1$ eV, which is shifted with respect to the Sn_B component appearing at $E = 25.5$ eV. This is the stanene related Sn_S , as shown by the red dashed lines. The significance of investigating the Sn $4d$ shallow core level is that the Sn_S component is observed as a distinct peak in both the Sn $4d$ spin orbit components (red double sided horizontal arrows in Fig. S14(a) of SM [66]) in contrast to Sn $3d_{5/2}$. This is because of smaller life time broadening of the Sn $4d$ core level as well as use of synchrotron radiation that result in better energy resolution. The Sn_S component is shifted from the Sn_B component in Sn $4d$ by 0.4 eV, which is nearly similar to that obtained for Sn $3d_{5/2}$ from curve fitting.

The spectra in Fig. S14 of the SM [66] also show the Bi $5d$ core level, which furthermore enables us to comment about the BL. The Bi $5d_{5/2}$ and $5d_{3/2}$ peaks for MBST ($t_d=0$) at $E = 24.8$ and 27.9 eV, respectively, represent the main component (Bi_M). As in case of Bi $4f_{7/2}$, an additional component (Bi_B) related to the BL appears for $t_d > 0$. This component at $E = 26.75$ eV is evidently for Bi $5d_{3/2}$ (blue dashed line), since it does not coincide with Sn $4d$. It is also observed for Bi $5d_{5/2}$ at similar separation, as shown by blue arrows. The separation between Bi_B and Bi_M is 1.15 eV, which is similar to that observed for Bi $4f_{7/2}$ [Fig. 2(d)]. Bi_B increases in intensity as the BL forms up to $t_d = 2.4$ -2.6 min and thereafter remains almost unchanged. The underlying Bi_M component is very weak for $t_d \geq 2.6$ min when the BL is fully formed, unlike in Bi $4f_{7/2}$, because enhanced surface sensitivity of the former with IMFP of 0.5 nm [65] compared to relatively less surface sensitive Bi $4f_{7/2}$ with IMFP of 2.9 nm.

C. STM study of stanene and the buffer layer

BL onset: At the initial stage of Sn deposition on MBST ($t_d = 1.2$ min), where both ARPES and XPS indicate the formation of BL without any signature of stanene, Fig. 3(a) shows that about 60% of the substrate is covered by the BL that are manifested as islands of height $h_b = 0.5 \pm 0.05$ nm measured from the uncovered Te top layer of MBST (dark brown region) (Fig. 3(b), see also the height histogram in Fig. S15(a) of the SM [66]). Thus, h_b is due to Sn deposition and is larger than the typical thickness of a Sn monolayer (0.18-0.38 nm) grown on different substrates [6–8, 16, 45, 46, 73]. Rather, h_b is close to twice the covalent diameter of Sn (0.278 nm [74]), indicating that two Sn atoms per unit cell would be required for BL formation, as has been shown earlier by its composition determined from XPS. Despite the admixture of Sn with Te and Bi/Sb in the BL islands caused by chemical bonding and anti-site defect formation, the validity

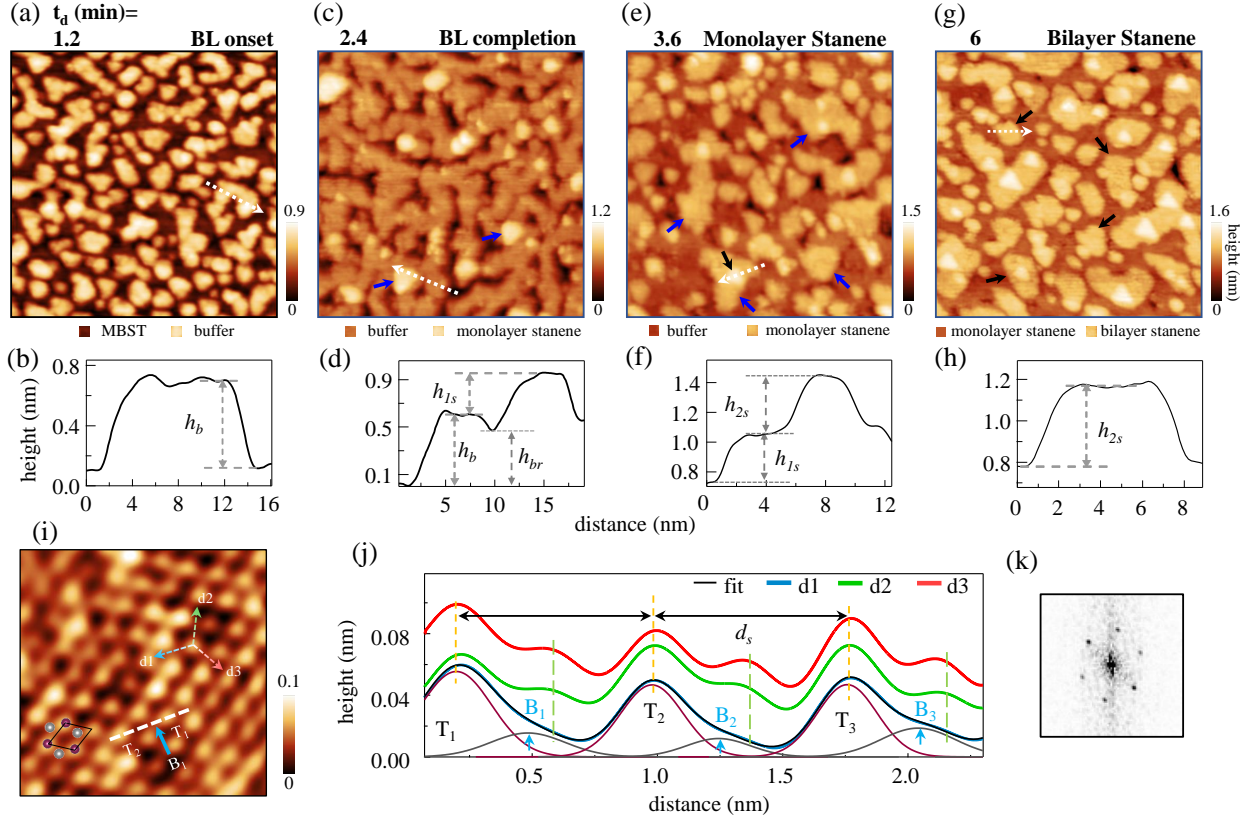


Figure 3. STM topography images of size $70 \text{ nm} \times 70 \text{ nm}$ for $t_d =$ (a) 1.2 min with $I_T = 0.4 \text{ nA}$ and $U_T = 1 \text{ V}$, (c) 2.4 min with $I_T = 0.14 \text{ nA}$ and $U_T = 0.07 \text{ V}$, (e) 3.6 min with $I_T = 0.9 \text{ nA}$ and $U_T = 0.4 \text{ V}$, and (g) 6 min with $I_T = 0.1 \text{ nA}$ and $U_T = 0.5 \text{ V}$. The legends at the bottom of each image indicate the color of the different regions. The blue [black] arrows in panels **c**, **e** [**e**, **g**] highlight the monolayer (bilayer) stanene islands. (b, d, f, h) Height profile along the white dashed arrow for panels **a**, **c**, **e**, and **g**, respectively. The heights of the BL, monolayer and bilayer stanene are represented by h_b , h_{1s} and h_{2s} , respectively. (i) An atomically resolved image of bilayer stanene ($4 \text{ nm} \times 4 \text{ nm}$, $I_T = 1.5 \text{ nA}$, $U_T = -0.5 \text{ V}$, $t_d = 6 \text{ min}$). (j) Average height profiles of panel **i** along d_1 , d_2 and d_3 directions. The curve along d_1 is fitted with Gaussian functions. White dashed line in panel **i** defines T_1 , B_1 and T_2 . Peaks marked by T_n ($n = 1-3$) (magenta curves, maxima shown by yellow dashed lines) represent the upper sublattice atoms of stanene. B_n (gray curves), whose peak positions are highlighted by blue arrows, represent the lower sublattice atoms that are shifted from $d_s/2$ (green dashed lines). (k) The Fourier transform of panel **i**.

of the aforementioned argument holds due to the similarity in their sizes [74]. The total thickness of the BL, including the thickness of the Te and Bi/Sb layers, is estimated to be $\sim 0.9 \text{ nm}$, where the

thickness of the top two layers of MBST is taken to be ~ 0.4 nm from x-ray crystallography [75].

BL completion: In Fig. 3(c) for $t_d = 2.4$ min deposition, the almost fully formed BL covers more than 90% of the substrate. Its height is similar to that of previous deposition, but there are some less darker regions, where the height is however smaller than 0.5 nm. An example of the reduced height of the BL is shown by h_{br} in the height profile [Fig. 3(d)]. This is also indicated by the asymmetry in the height histogram around 0.3 nm in Fig. S15(b) of SM [66]. Thus, the BL has a somewhat non-uniform thickness. This is reflected by its enhanced mean square roughness (S_q) of $0.12 (0.14) \pm 0.025$ nm at $t_d = 1.2 (2.4)$ min estimated by masking the uncovered substrate.

Monolayer stanene: In Fig. 3(c), blue arrows indicate the presence of a few bright islands on the BL that have a step height of h_{1s} and cover $\sim 10\%$ of the area. Note that at this t_d of 2.4 min, signature of stanene formation is also visible from XPS [Fig. 2(a)]. At $t_d = 3.6$ min, these islands increase in size with similar h_{1s} that covers about 65% of the BL [blue arrows in Fig. 3(e)]. Based on the height profile shown in Fig. 3(f) and the histogram in Fig. S15(c) of the SM [66], it can be concluded that the value of h_{1s} is 0.35 ± 0.02 nm, suggesting that the observed islands are composed of a monolayer of stanene. This is corroborated by the height profile analysis of the atomic resolution image depicted in Fig. S16 of the SM [66]. Subsequently, this will be elaborated upon, particularly in relation to bilayer stanene in Figs. 3(i) and 3(j). In Fig. 3(e), the regions that are not covered by monolayer stanene represent the BL. These BL regions are smoother with $S_q = 0.08 \pm 0.01$ nm compared to Fig. 3(c). In fact, the smoothness of the BL here is comparable to the substrate ($S_q = 0.07 \pm 0.01$ nm). An atomic resolution STM image of the BL region in Fig. S17 of the SM [66] shows an ordered structure, as also indicated by LEED (Fig. 4).

Bilayer stanene: Figure 3(e) shows evidence of small islands on monolayer stanene, one of these is highlighted by a black arrow. These islands cover about 3% area, but grow in size and number with further Sn deposition [$t_d = 6$ min, Fig. 3(g), islands shown by black arrows] covering more than $\sim 60\%$ of the total area. The height of these Sn islands (h_{2s}) shown by height profiles along the white dashed lines in Figs. 3(f) and 3(h) is 0.35 ± 0.03 nm. The difference between the two peaks of the height histogram in Fig. S15(d) of SM [66] also agrees with this estimate. Note that h_{2s} is similar to h_{1s} indicating formation of bilayer stanene. Its growth commences on the monolayer stanene islands prior to the latter's complete coverage of the BL, which is a characteristic of Stranski-Krastanov (SK) growth.

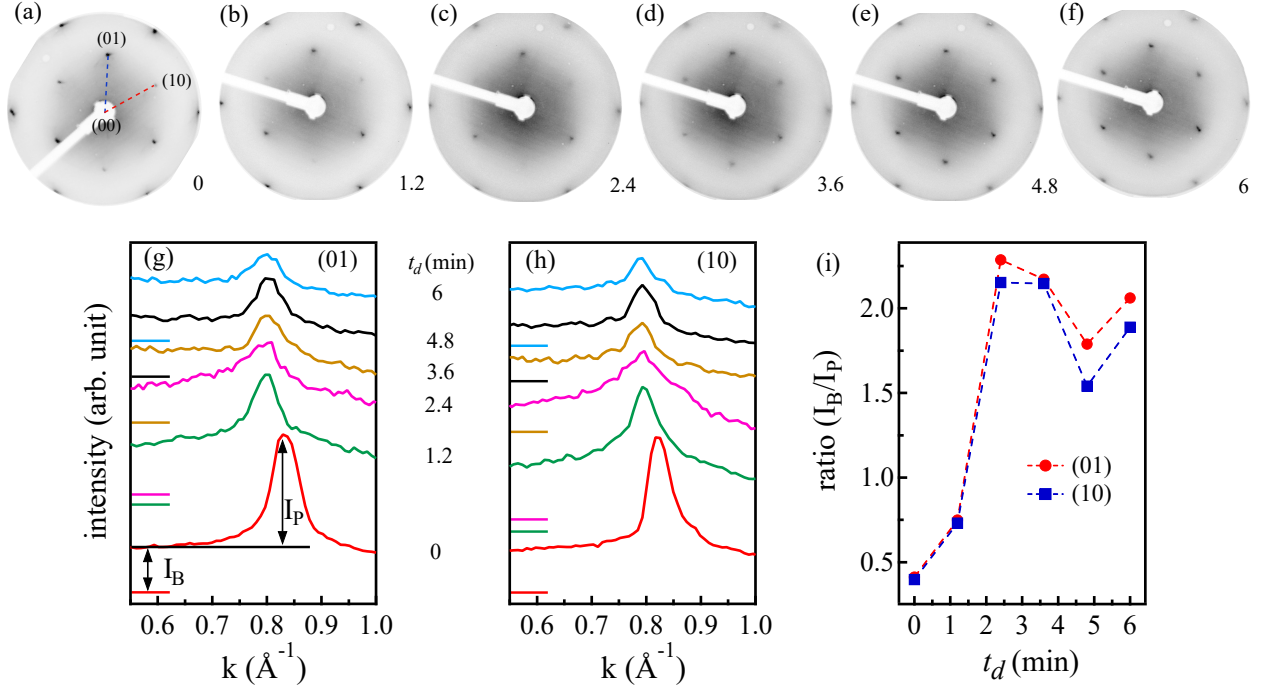


Figure 4. (a-f) A set of LEED patterns in inverted gray scale with primary electron beam energy (E_p) of 55 eV, t_d in min is indicated at the lower right corner of each panel. The intensity profiles from the LEED patterns in panels **a-f** along (g) (00) to (01) spot [blue dashed line in panel **a**] and (h) (00) to (10) [red dashed line in panel **a**]. All the profiles are staggered in the vertical direction and are aligned to (00) at the center of the pattern that is covered by the shadow of the electron source. The zero of each profile is shown by a short horizontal line of same color on the left vertical axis. (i) Ratio of the background intensity (I_B) and intensities of the (01) and (10) spots (I_P), measured as shown in panel **g**.

The step height of 0.35 nm determined above is close to the step height (0.35-0.36 nm) of stanene on other substrates such as Bi_2Te_3 [6] and PbTe [10], where buckling of 0.09-0.12 nm was reported. Zhu *et al.* [6] determined buckling height from a step height between the upper and lower stanene sublattice. Following a similar approach, we find the buckling height of stanene on MBST to be 0.1 ± 0.015 nm (Fig. S18 of SM [66]). The different structural parameters, such as lattice constant, step height, and buckling height, determined in this work are compared to those on other substrates in the literature in Table I. According to Table I, the structural characteristics of stanene on MBST are similar to those of other chalcogenide substrates with Te termination, such as Bi_2Te_3 [6] and PbTe [10].

Atomic resolution image of stanene: An atomic resolution image of a bilayer stanene island is shown in Fig. 3(i), where the unit cell (black line) joins four Sn atoms visible as bright spots (magenta circles) of the upper sublattice (represented by T_n). The lower sublattice atoms are shown by gray circles and represented by B_n . In Fig. 3(j), the average height profiles along d1, d2 and d3 directions 120° apart are shown staggered along the vertical axis. These directions are shown in Fig. 3(i). In addition Fig. S19 of SM [66] shows all the parallel dashed lines in each direction over which averaging was performed. These height profiles show distinct peaks related to T_n and shoulders related to B_n , $n= 1-3$. In order to ascertain their positions, Gaussian functions with nearly similar full width at half maxima have been used to fit the profile. The quality of the fitting is good, as shown by the fitted curve in Fig. 3(j).

A confirmation that Fig. 3(i) represents stanene is based on the observation that B_n related peaks (gray curves, peak position highlighted by blue arrows) are not at $d_s/2$ [green dashed vertical line at the mid points of T_n and T_{n+1} in Fig. 3(j)], but is closer to T_n 's. This asymmetry is the signature of stanene formation that stems from the contribution of intensity to B_n by the Sn atoms in the lower sublattice. An atomic resolution image for monolayer stanene ($t_d= 3.6$ min) analyzed in a similar way also shows this behavior (Fig. S16 of SM [66]).

The average separation between T_n and B_n related peaks is 0.34 ± 0.04 nm. This is comparable to the ideal value of $d_s/3$ ($= 0.27$ nm) obtained when a buckled hexagon is projected on the horizontal plane. The average separation between T_n and T_{n+1} is $d_s = 0.8\pm 0.02$ nm, which is the longer diagonal of the primitive unit cell. d_s is related to the lattice constant a_s by $d_s/\sqrt{3}$, which turns out to be 0.46 ± 0.01 nm. A similar value of a_s is also obtained from the Fourier transform shown in Fig. 3(k). It is worth noting that a_s is close to that of freestanding stanene (0.467 nm) [2, 3]. The unequal heights of the upper (T_n) and the lower sublattice (B_n) from our height profile analysis is also an indication of buckling in stanene.

MBST substrate: Figures S20(a,b) of the SM [66] show a wide area topography image of MBST, where the step height of 1.4 ± 0.03 nm corresponds to the height of a septuple layer. A similar analysis, as discussed above for stanene, has been performed for an atomic resolution STM image of MBST in Figs. S20(c) and S20(d) of the SM [66]. Curve fitting of the height profiles along d1-d3 shows that, unlike stanene, the shoulder labeled by R is at $d_s/2$ i.e., at the middle of $T_n T_{n+1}$. R is attributed to the residual contribution of the Te atoms connected by the smaller diagonal of the unit cell shown in Fig. S20(c) of SM [66] by dashed blue lines. The lattice constant of MBST is determined to be 0.44 ± 0.01 nm, which agrees well with x-ray diffraction result (0.430 nm for

TABLE I. The lattice constant, step height and buckling height (in nm) of stanene on MBST compared with stanene on other substrates ([†]lattice matched with substrate, [‡]DFT value, ^{††}(2×2) structure).

Name of substrate [Reference]	Lattice constant	Step height	Buckling height
free standing [2, 3]	0.467 [‡]	–	0.085 [‡]
MBST [our work]	0.46±0.01	0.35±0.03	0.1±0.015
Bi ₂ Te ₃ [6]	0.438 [†]	0.35±0.02	0.12±0.02
PbTe [9, 10]	0.452 [†]	0.36	0.093 [‡]
Bi [8, 76]	0.454 [†]	0.4	0.13
InSb [45]	0.462	0.35	–
Sb [46]	0.43 [†]	0.51±0.01	–
Pd [15]	0.48	–	0.02
Cu [7]	0.51 ^{††}	0.18	0

~30% Sb-doped MBST) [75]. The uniformity of the Sb doping in MBST is demonstrated by the resemblance of scanning tunneling spectra, which depict the local density of states, at various spatial positions, as shown in Figs. S20(e) and S20(f) of the SM [66]. Interesting to note is that the lattice constant of stanene (0.46 nm) turns out to be larger than MBST. This lattice mismatch is bridged by the BL, as shown by our LEED study presented below.

D. Low energy electron diffraction for different t_d

A set of LEED patterns in Figs. 4(a) to 4(f) demonstrate epitaxial growth for all depositions, in spite of the BL formation. Sharp (1×1) spots are observed for the beam energy (E_p) range $41\text{ eV} < E_p < 130\text{ eV}$ without any splitting or streaking. The symmetry of the BL remains similar to the substrate, as shown by Figs. 4(a) to 4(c). The intensity profiles along (00) to (01) spot [Fig. 4(g)] and (00) to (10) spot [Fig. 4(h)] i.e., along the blue and red dashed lines, respectively, do not show any splitting. There is however a shift in the positions of both the (01) and (10) spots: the peaks in the corresponding intensity profiles for stanene e.g., for $t_d \geq 3.6$ min are shifted towards lower k by similar amount compared to that of MBST ($t_d = 0$ min). This shows a decrease in their separation with the (00) spot ($k = 0$). This indicates that the lattice constant of stanene is larger compared to MBST. This increase is estimated to be $3.1\% \pm 0.5\%$ considering more than 80 intensity profiles of different E_p 's for $t_d = 3.6\text{--}6$ min (the lattice constants of monolayer and bilayer stanene are similar). The lattice constants of stanene and MBST determined by STM are consistent with the LEED results. Figures 4(g,h) further show that when the BL formation is completed ($t_d = 2.4$ min), both the (01) and (10) peaks are nearly aligned to that of stanene i.e., are shifted towards lower k . This indicates that the lattice constant of the BL is larger than MBST by $3\% \pm 0.5\%$. Thus, the lattice constant of the BL is similar to that of stanene within the error. This shows that the lattice mismatch between stanene and MBST is bridged by the BL. A similar role of the BL has been reported in the case of Bi_2Se_3 grown on 2H-NbSe_2 substrate [77, 78].

An additional important observation from Figs. 4(a) to 4(f) is that the background to the spot intensity ratio increases quite substantially for the BL compared to MBST, as quantified in Fig. 4(i) from the ratio of the background (I_B) and the spot (I_P) intensities. This ratio is maximum at $t_d = 2.4$ min where the BL is fully formed. Such an increase in the background intensity in the LEED pattern has been related to the existence of random anti-site defects in previous literature [79, 80]. $(\text{Bi/Sb})_{\text{Te}}$ anti-site defects, where Bi/Sb atoms of the second layer are exchanged with the Te atoms of the top layer, are already present in MBST. In agreement with previous literature [81, 82], signature of $(\text{Bi/Sb})_{\text{Te}}$ anti-site defect has been observed as bright circular spot in the STM image (red dashed circles in Fig. S20(c) of the SM [66]). With Sn deposition, the anti-site defects are enhanced, possibly because of the propensity for chemical bonding aided by the kinetic energy of the impinging Sn atoms (equal to 1073 K) and the closeness of their atomic diameters (0.278 nm, 0.276 nm, 0.296 nm, and 0.278 nm for Sn, Te, Bi, and Sb, respectively [74]).

E. Band dispersion and Fermi surface from ARPES

The ARPES intensity plots of predominantly monolayer stanene that almost completely covers the BL at $t_d=4.8$ min are depicted in Figs. 5(a) to 5(d). Some monolayer regions are covered by an additional stanene layer, i.e., bilayer stanene as a result of SK growth, as demonstrated by STM. These measurements have been performed at 80 K after deposition at room temperature with statistics better than that of Fig. 1(h).

Bands around the $\bar{\Gamma}$ point and the Fermi surface: Figure 5(a) shows two bands, outer and inner, towards the $\bar{\Gamma}$ - \bar{M} direction. Their dispersion is hole-like, as shown by red open circles for the outer band. These circles correspond to the maximum intensity of the momentum distribution curves (MDCs) obtained from Fig. 5(a) at different E (Fig. S21 of the SM [66] shows how the maxima of the MDCs are identified by fitting). The red dashed line, which is a linear fit to the red circles, shows that the dispersion is a close approximation to linearity. The inner hole band (green dashed line), determined in a similar way, disperses down to 0.8 eV at 0.4 \AA^{-1} . An inverted parabolic band is also observed that disperses from a maximum E of ~ 0.4 eV at $\bar{\Gamma}$ to 0.8 eV at $\sim 0.2 \text{ \AA}^{-1}$. A second derivative ARPES intensity plot in Fig. 5(b) shows these bands prominently.

To probe whether the outer band crosses E_F , we have deposited potassium (K), which provides electrons to the surface that would fill up this band [6, 83]. Thus, the band positions above E_F can be determined. As shown by the red filled circles in Fig. 5(a) (the corresponding ARPES intensity plots shown in Fig. S22 of the SM [66]), we find that the outer band crosses E_F .

The outer and inner stanene bands towards the $\bar{\Gamma}$ - \bar{K} direction are observed in Figs. 5(c) and 5(d), which are highlighted by open circles and the dashed curves. ARPES data in an extended range (\bar{M} - $\bar{\Gamma}$ - \bar{K}) taken at room temperature are shown in Fig. S23 of SM [66], with the bands obtained above overlaid. The Fermi surface shown in Fig. 5(e) exhibits hexagonal symmetry, where k_F is 0.4 \AA^{-1} towards \bar{K} compared to 0.35 \AA^{-1} towards \bar{M} . Such hexagonal Fermi surface of stanene has been observed on Bi_2Te_3 [44] and Pd_2Sn [15]. A series of k_x - k_y isosurface plots for E varying from 0.1 to 0.4 eV in Fig. S24 of the SM [66] also exhibits the hexagonal symmetry. Interestingly, segmentation of the isosurface plots indicate formation of nodes at \bar{K} and \bar{M} that could possibly be related to band crossings.

Note that the Fermi velocities of stanene (estimated from the slope of the outer band) towards $\bar{\Gamma}$ - \bar{M} and $\bar{\Gamma}$ - \bar{K} are similar, i.e., $3.2 \pm 0.02 \times 10^5$ m/s. This value is somewhat larger compared to

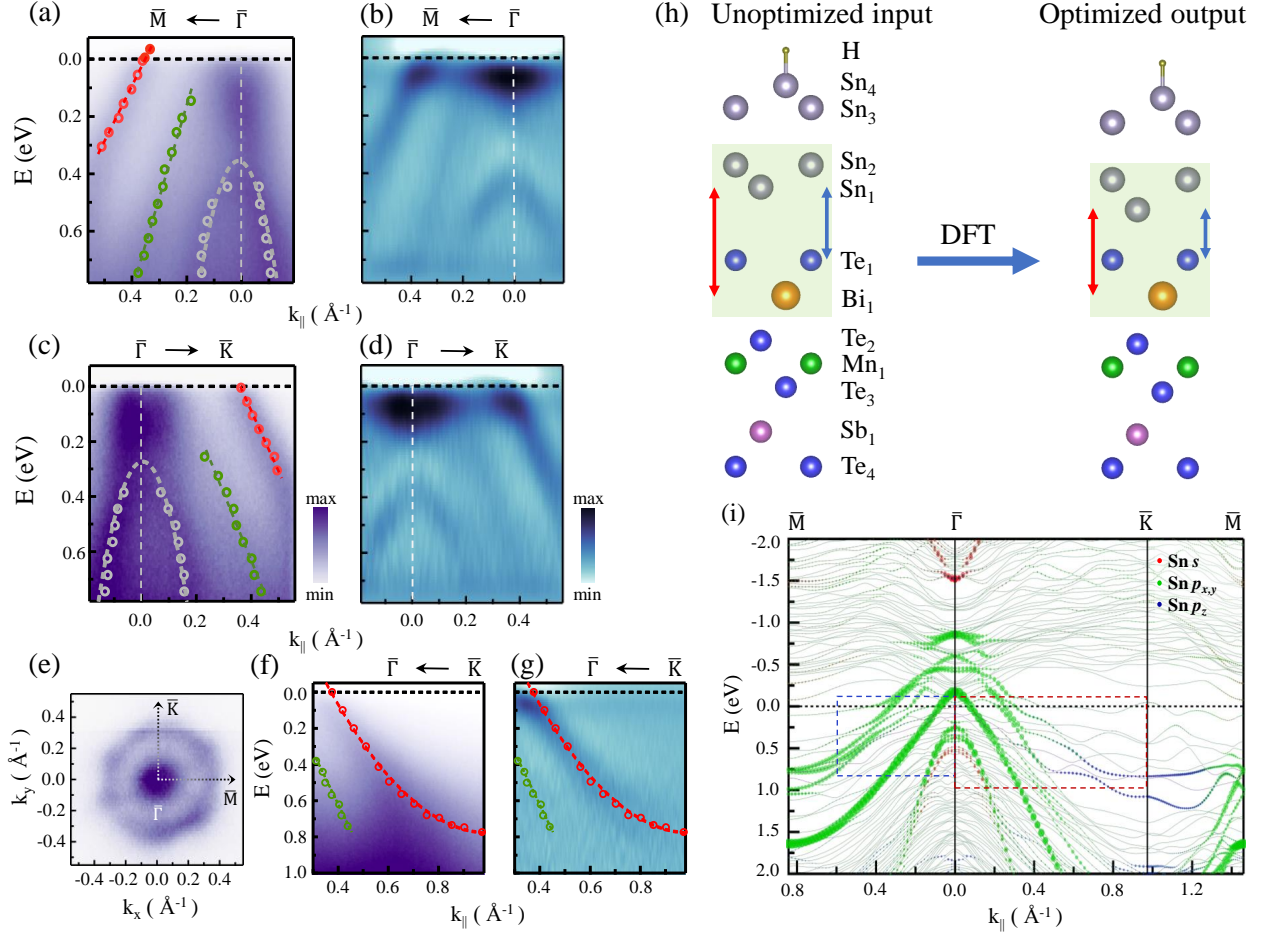


Figure 5. ARPES intensity plots of predominantly monolayer stanene from $\bar{\Gamma}$ towards (a) \bar{M} and (c) \bar{K} directions. The BZ is shown in the inset of Fig. 1(a). Open circles (red: outer band, green: inner band and gray: inverted parabolic band) represent the positions of the bands obtained by fitting the MDCs. The dashed curves are obtained by fitting the open circles. (b, d) Second derivative image of panels a and c, respectively. (e) The Fermi surface of stanene obtained from ARPES after averaging over ± 15 meV. (f) Raw and (g) second derivative ARPES intensity plot toward the $\bar{K}-\bar{\Gamma}$ direction. In panel f, the red circles and the dashed curve are obtained from fitting and these are overlaid on panel g. (h) The unoptimized input (left panel) and the optimized output (right panel) structures of “S+BL+H” DFT calculation for monolayer stanene on MBST including BL (green shading) and H passivation (topmost layer). Both the structures have been drawn in the same scale using the VESTA program [61]. The labeled atoms are represented by size-scaled circles of various colors. The blue (red) double arrow indicates the Sn₁-Te₁ (Sn₁-Bi₁) layer separation. (i) The $E - k_{\parallel}$ band dispersion calculated including SOC for “S+BL+H” along $\bar{M}-\bar{\Gamma}-\bar{K}-\bar{M}$ direction. The bands of Sn $p_{x,y}$, p_z , and s character are shown. Blue (red) dashed rectangle shows the range measured in ARPES towards \bar{M} in panel a (\bar{K} in panels c, f).

stanene on Bi₂Te₃ (2.79×10^5 m/s) [44] or Sb₂Te₃ (2.83×10^5 m/s) [84], indicating that stanene on MBST may be useful in high-speed electronic devices.

Bands around the \bar{K} point: Figures 5(f,g) show the outer hole band up to the \bar{K} point. This band crosses the \bar{K} point at ~ 0.8 eV, as shown by the red circles and dashed curve obtained from fitting the raw data in panel f. No other bands are observed near E_F , thus indicating a bandgap of 0.8 eV at the \bar{K} point. This behavior is in contrast to freestanding stanene, where this band disperses towards E_F due to the π - π bonding between the unsaturated Sn p_z orbitals and opens a nontrivial band gap of 0.1 eV [2, 3].

The above discussed deviation of the ARPES band dispersion at the \bar{K} point has been reported earlier for stanene grown on telluride substrates [6, 9, 10], where an experimental band was likewise shifted to higher E opening up a large bandgap. On the contrary, the DFT calculations for stanene including the substrate showed absence of the gap, unless hydrogen passivation was considered [6, 8–10]. It was argued that hydrogen passivates the reactive Sn p_z orbital, and this is possible in ultra high vacuum chambers made of stainless steel because hydrogen is the dominant residual gas [85, 86]. Residual gas analysis conducted with a quadrupole mass spectrometer indicates that hydrogen is the most prevalent gas in our chamber (Fig. S25 of SM [66]). This mass spectrum is comparable to that of Ref. 8, in which hydrogen passivation of stanene was demonstrated and the chamber pressure was nearly identical to ours. The probability of hydrogen passivation is evident when we estimate the number of hydrogen molecules at a pressure of 1×10^{-10} mbar to be $\sim 2.5 \times 10^{12}/\text{m}^3$. Additionally, being the lightest gas, hydrogen has the highest molecular speed among all the gases.

F. DFT calculation for stanene on MBST

Input structure for DFT calculation: The left panel of Fig. 5(h) shows the input structure for DFT calculation, where buckled monolayer stanene is represented by an upper sublattice (Sn₄) and a lower sublattice (Sn₃). The BL is modeled based on the information about its composition and symmetry obtained from XPS, LEED, and STM; random anti-site disorder is, however, not considered. The BL is represented by two Sn sublattices similar to stanene (Sn₂ and Sn₁, where the upper Sn₂ sublattice is at the fcc site) and the top Te (Te₁) and Bi (Bi₁) layers of MBST, as shown by the green shading. The Sn layers of BL and stanene resemble the α -Sn structure in the (111)

direction. Hydrogen (H) passivation is considered in our calculation for the reasons discussed at the end of the previous section (III.E). The H atom is placed at the on top position at a distance of 0.176 nm from Sn₄ [see Fig. S26(a) for all the interlayer separations]. The substrate MBST(0001) is represented by its unit cell (Fig. S3(a) of SM [66]) with three septuple layers, where 2 of the 6 Bi atoms were replaced by Sb so that the doping level is 33%, which is close to the experiment. The lattice constant is taken to be 0.430 nm based on x-ray crystallography data [75]. The atom positions have been fully relaxed for stanene, BL, H, and the top septuple of MBST, whereas the two bottom septuples were kept fixed.

Optimized output structure from DFT : The output structure in the right panel of Fig. 5(h) shows significant change in separation of the layers representing the BL (green shading) (also see Fig. S26(b) of the SM [66]). Particularly, Sn₁ shifts down and the inter layer separation between the Sn₁ and Te₁ layers (Sn₁-Te₁ distance along the z direction shown by blue double arrow) decreases substantially to 0.25 nm from the starting value of 0.365 nm (which is the separation for stanene on PbTe after optimization, where BL is not present [10]) . Consequently, the distance between Sn₁ and Te₁ atoms considering their (x, y, z) coordinates reduces to 0.353 nm from 0.44 nm before optimization. This distance is close to that of SnTe (0.316 nm) [87]. Thus, the formation of a chemical bond between Sn₁ and Te₁ can be suggested. The Sn₂-Te₁ distance also decrease from 0.472 nm to 0.395 nm. Similar to the Te₁ layer, the Sn₁-Bi₁ layer distance (red double arrow) is reduced by 0.111 nm (from 0.54 to 0.429 nm). A substantial decrease in the interlayer separations between Sn and the top two atomic layers of the MBST substrate, is the signature of BL formation from DFT. Due to this, the separation between the Bi₁ and the underlying Te₂ layer increases slightly from 0.223 to 0.238 nm. The Te₂-Mn₁ layer separation remain almost unchanged, indicating that these layers are not part of the BL.

After optimization, stanene shows a buckling height of 0.124 nm given by Sn₄-Sn₃ separation, which is in good agreement with STM (0.1 ± 0.015 nm). Additionally, the separation between stanene and the BL, i.e., the Sn₃-Sn₂ separation (0.284 nm), remains almost unchanged. For comparison with the other DFT calculation discussed later, we annotate this calculation as “**S+BL+H**”, where both BL and H passivation are considered (“**S**” stands for monolayer stanene).

DFT band structure for S+BL+H calculation: Figure 5(i) shows the stanene related bands for the above discussed structure. Two adjacent bands of Sn p_z orbital character are found to traverse

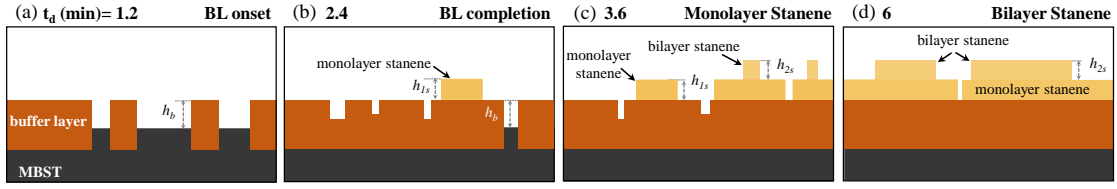


Figure 6. (a-d) A set of schematic diagrams showing the growth of monolayer and bilayer stanene (yellow) on the BL (reddish brown). h_b , h_{1s} , h_{2s} represent the heights of the BL, monolayer stanene and the bilayer stanene, respectively. The MBST substrate is shown in black color.

the \bar{K} point at $E = 0.85$ and 1.1 eV. Thus, the bandgap at the \bar{K} point is measured to be 0.85 eV, which closely matches the bandgap of 0.8 eV from ARPES [Figs. 5(f) and 5(g)]. These bands disperse up towards E_F and approach the $\bar{\Gamma}$ point, and constitute the outer hole band that is observed in ARPES [Figs. 5(c, d, f, g)]. The Sn $p_{x,y}$ orbital character (green circles) of the bands is apparent below 0.5 \AA^{-1} . The outer hole band of Sn $p_{x,y}$ character is also observed towards the \bar{M} point, which shows a minimum around 1 eV at \bar{M} . DFT also exhibits the inner hole band found in ARPES about $\bar{\Gamma}$. It is of $p_{x,y}$ character and crosses E_F from both \bar{M} and \bar{K} directions at 0.07 \AA^{-1} and shows a maximum at 0.2 eV above E_F . It shows a minimum at 1.6 eV at \bar{M} and disperses to >2 eV towards \bar{K} .

Besides the outer and inner bands, the inverted parabolic band observed in ARPES is also observed in both directions, with a maximum at $\bar{\Gamma}$ at ~ 0.4 eV. It has primarily $p_{x,y}$ character with approximately equal contributions from the p_x and p_y orbitals, with some admixture of s character (Fig. S27 of SM [66]). The outer and inner hole bands also have nearly similar p_x and p_y contributions. A primarily Sn s band appears above E_F with a minimum at $E = -1.5$ eV around the $\bar{\Gamma}$ point. Stanene on MBST is found to be metallic, where both the inner and outer bands cross E_F around $\bar{\Gamma}$ and give rise to the outer hexagonal and inner circular pocket of the Fermi surface, respectively [Fig. 5(e)].

The preceding discussion demonstrates a good agreement between ARPES [Figs. 5(a) to 5(g)] and DFT [Fig. 5(i)]. The bandgap at \bar{K} is reproduced, and all the bands appear in the latter. However, unlike freestanding stanene, the Dirac cone at the \bar{K} point is absent due to the bandgap, and band inversion is not observed. Therefore, the non-trivial band structure is not observed for stanene on MBST, as is also the case for stanene on Bi_2Te_3 [6] and PbTe [10].

S+BL DFT calculation: To examine the role of H passivation, another calculation has been performed with the input structure as in the left panel of Fig. 5(h), but with the H layer removed. It is referred to as the “**S+BL**” calculation. The resulting optimized structure in Fig. S28(a) of SM [66] shows BL formation with reduced Sn₁-Te₁ (0.25 nm) and Sn₁-Bi₁ (0.435 nm) separations. These values are close to the **S+BL+H** calculation (Fig. S26(b) of SM [66]). Therefore, the absence of H passivation does not influence the BL formation. On the other hand, stanene demonstrates a notable increase of ~28% to 0.159 nm in the buckling height, which is observed from the Sn₄-Sn₃ separation. This enhances the hybridization between the unpassivated p_z and the $p_{x,y}$ orbitals [2] and influences the band structure (Fig. S28(b) of SM [66]). The maximum of the inner (outer) hole band of Sn $p_{x,y}$ character moves up in E by about 0.7 (0.5) eV to above E_F . The inverted parabolic band that is of $p_{x,y}$ character shows a p_z contribution near the maximum due to the enhanced hybridization. Here too, the maximum is shifted to $E = -0.4$ eV. In contrast, the p_z bands around \bar{K} are shifted to $E = 0.6$ eV. Thus, the bands of the $p_{x,y}$ (p_z) character are shifted up (down) as a result of the stabilization of the stanene structure with larger buckling and the resulting increase in the $p_{x,y}$ - p_z hybridization.

BL+H DFT calculation: A calculation conducted using a monolayer stanene structure that is passivated with hydrogen [Fig. S29(a)] results in an optimized structure where the distances between Sn₁-Te₁ (0.25 nm) and Sn₁-Bi₁ (0.43 nm) significantly decrease. This indicates that the stanene transforms to the BL structure (Fig. S29(b) of the Supplementary Material [66]). So, the optimized structure can be regarded as the BL without a stanene (**S**) layer, and is termed as the “**BL+H**” calculation. This calculation shows the importance of the BL, in the absence of which stanene will exhibit chemical bonding with the top two layers of the substrate and the stanene related bands might not be observed. Indeed, Fig. S29(c) of SM [66] shows that the stanene related inner and parabolic bands are absent. Nevertheless, a Sn related band resembling the outer band is observed in theory. However, the random anti-site disorder present in the BL, which is not considered in our calculation, is expected to broaden and thus weaken this band. So, this band is faint in the raw data in Fig. 1(f), but can be identified in the second derivative plot (white arrows in Fig. S4(f) of SM [66]) towards the \bar{M} direction for $t_d = 2.4$ min, when the BL formation is nearly completed and there is minimal stanene formation.

Thus, based on the three DFT calculations discussed above (**S+BL+H**, **S+BL**, and **BL+H**), it can be concluded that the stanene band structure calculated with both BL and H passivation yields

good agreement with ARPES, as seen from the results of the **S+BL+H** calculation presented in Figs. 5(h) and 5(i).

IV. CONCLUSION

In conclusion, using a combination of complementary analytical techniques and density functional theory (DFT), we report the formation of stanene on a magnetic topological insulator (MBST), whose growth is aided by the formation of an underlying BL. The whole sequence of growth as a function of Sn deposition time (t_d) is depicted in Fig. 6 through a series of schematic representations. For the initial depositions, angle resolved photoemission spectroscopy (ARPES) shows a gradual shift of the MBST valence band, indicating electron transfer to the substrate. This is the onset of the BL formation [Fig. 6(a)], as shown also by scanning electron microscopy (STM) and core level spectroscopy. Stanene formation starts on the BL [Fig. 6(b)], the latter having a thickness of 0.9 nm and a composition of Sn:Te:Bi/Sb \approx 2:1:1. Low energy electron diffraction (LEED) and STM show that the BL has an ordered crystal lattice, albeit with random anti-site defects.

The height profile analysis of the atomic resolution STM images provides evidence for both monolayer and bilayer stanene. The stanene layers develop in the form of islands, exhibiting a Stranski-Krastanov growth mode with a step height of 0.35 ± 0.03 nm [Figs. 6(c) and 6(d)]. The buckling height is estimated from STM to be 0.1 ± 0.015 nm. The LEED intensity profiles indicate that the lattice constant of stanene is $\sim 3.1\%$ larger than that of MBST, which aligns with the findings from STM. The BL bridges this disparity and provides a platform for stanene growth. A stanene-related component is detected in the Sn d core level spectra in addition to a BL-related component.

ARPES intensity plots and DFT calculations for monolayer stanene (the **S+BL+H** calculation) show hole-like inner and outer bands and an inverted parabolic band around the $\bar{\Gamma}$ point of primarily Sn $p_{x,y}$ orbital character. The outer band traverses the E_F showing that stanene is metallic with a Fermi surface of hexagonal symmetry. In contrast, a bandgap of 0.8 eV is observed at the \bar{K} point, where the outer band is of Sn p_z orbital character. We find that DFT band structure calculations show good agreement with the ARPES only when the BL and H passivation are considered in the calculation. From this calculation, all the bands are identified, and a nearly similar bandgap at the \bar{K} point is obtained. On the other hand, if either BL or H passivation are not considered in the

calculation, the agreement is unsatisfactory.

Formation of stanene opens up the possibility of superconductivity [8, 9] and its ensuing proximity effect with MBST. The proximity effect could be tuned by varying the thickness of the BL through modification of the growth conditions. The BL could also possibly become superconducting, as there are reports in literature about superconductivity in $\text{Sn}_{0.57}\text{Sb}_{0.43}$ with $T_C = 1.45$ K [88] and $\text{Sn}_{1-\delta}\text{Te}$ with $T_C < 0.3$ K [89], both having rhombohedral structure as is the case here. Despite the presence of the BL, the magnetic interaction due to the Mn layer of the substrate could potentially impact the properties of stanene because the separation of the latter from the Mn layer (~ 1.3 nm, Fig. S26(b) of SM [66]) is smaller than the magnetic interaction range (≥ 3.36 nm [90, 91]). Our work establishes the formation of stanene on a magnetic topological insulator, which may lead to an interesting interplay between band topology, superconductivity, and magnetism.

Acknowledgments

The Computer division of Raja Ramanna Centre for Advanced Technology is thanked for installing the DFT codes and providing support. R.B. would like to acknowledge the partial support from the Start-up Research Grant (SRG), SERB, Govt. of India, file no. SRG/2022/000552-G. A.P. acknowledges the Israel Council for Higher Education for a postdoctoral fellowship through the Study in Israel program. M.H. thanks the Leona M. and Harry B. Helmsley Charitable Trust grants 2018PG-ISL006 and 2112-04911 for support. M.B. and S.R.B. are thankful for the support from Science and Engineering Board through a CRG project (CRG/2023/001719). We are thankful to A. Gloskovskii for support during the HAXPES measurement. The authors acknowledge the India@DESY collaboration and the CERIC-ERIC Consortium for financial support and access to Petra-III and Elettra synchrotron facilities, respectively.

*electronic address: barmansr@gmail.com

-
- [1] C.-C. Liu, H. Jiang, and Y. Yao, *Low-energy effective Hamiltonian involving spin-orbit coupling in silicene and two-dimensional germanium and tin*, Phys. Rev. B **84**, 195430 (2011).
- [2] Y. Xu, B. Yan, H.-J. Zhang, J. Wang, G. Xu, P. Tang, W. Duan, and S.-C. Zhang, *Large-Gap Quantum Spin Hall Insulators in Tin Films*, Phys. Rev. Lett. **111**, 136804 (2013).

- [3] L. Matthes, O. Pulci, and F. Bechstedt, *Massive Dirac quasiparticles in the optical absorbance of graphene, silicene, germanene, and tinene*, J. Phys.: Condens. Matter. **25**, 395305 (2013).
- [4] K. S. Novoselov, A. K. Geim, S. V. Morozov, D. Jiang, Y. Zhang, S. V. Dubonos, I. V. Grigorieva, and A. A. Firsov, *Electric Field Effect in Atomically Thin Carbon Films*, Science **306**, 666 (2004).
- [5] A. K. Geim and K. S. Novoselov, *The rise of graphene*, Nat. Mater. **6**, 183 (2007).
- [6] F.-f. Zhu, W.-j. Chen, Y. Xu, C.-l. Gao, D.-d. Guan, C.-h. Liu, D. Qian, S.-C. Zhang, and J.-f. Jia, *Epitaxial growth of two-dimensional stanene*, Nat. Mater. **14**, 1020 (2015).
- [7] J. Deng, B. Xia, X. Ma, H. Chen, H. Shan, X. Zhai, B. Li, A. Zhao, Y. Xu, W. Duan, S.-C. Zhang, B. Wang, and J. G. Hou, *Epitaxial growth of ultraflat stanene with topological band inversion*, Nat. Mater. **17**, 1081 (2018).
- [8] C. Zhao, L. Li, L. Zhang, J. Qin, H. Chen, B. Xia, B. Yang, H. Zheng, S. Wang, C. Liu, Y. Li, D. Guan, P. Cui, Z. Zhang, and J. Jia, *Coexistence of Robust Edge States and Superconductivity in Few-Layer Stanene*, Phys. Rev. Lett. **128**, 206802 (2022).
- [9] M. Liao, Y. Zang, Z. Guan, H. Li, Y. Gong, K. Zhu, X.-P. Hu, D. Zhang, Y. Xu, Y.-Y. Wang, K. He, X.-C. Ma, S.-C. Zhang, and Q.-K. Xue, *Superconductivity in few-layer stanene*, Nat. Phys. **14**, 344 (2018).
- [10] Y. Zang, T. Jiang, Y. Gong, Z. Guan, C. Liu, M. Liao, K. Zhu, Z. Li, L. Wang, W. Li, C. Song, D. Zhang, Y. Xu, K. He, X. Ma, S.-C. Zhang, and Q.-K. Xue, *Realizing an Epitaxial Decorated Stanene with an Insulating Bandgap*, Adv. Funct. Mater. **28**, 1802723 (2018).
- [11] L. Fu and C. L. Kane, *Superconducting Proximity Effect and Majorana Fermions at the Surface of a Topological Insulator*, Phys. Rev. Lett. **100**, 096407 (2008).
- [12] T. Shoman, A. Takayama, T. Sato, S. Souma, T. Takahashi, T. Oguchi, K. Segawa, and Y. Ando, *Topological proximity effect in a topological insulator hybrid*, Nat. Commun. **6**, 6547 (2015).
- [13] C. X. Trang, N. Shimamura, K. Nakayama, S. Souma, K. Sugawara, I. Watanabe, K. Yamauchi, T. Oguchi, K. Segawa, T. Takahashi, Y. Ando, and T. Sato, *Conversion of a conventional superconductor into a topological superconductor by topological proximity effect*, Nat. Commun. **11**, 159 (2020).
- [14] S. Charpentier, L. Galletti, G. Kunakova, R. Arpaia, Y. Song, R. Baghdadi, S. M. Wang, A. Kalaboukhov, E. Olsson, F. Tafuri, D. Golubev, J. Linder, T. Bauch, and F. Lombardi, *Induced unconventional superconductivity on the surface states of Bi_2Te_3 topological insulator*, Nat. Commun. **8**, 2019 (2017).
- [15] J. Yuhara, T. Ogikubo, M. Araidai, S.-i. Takakura, M. Nakatake, and G. Le Lay, *In-plane strain-free*

- stanene on a Pd₂Sn(111) surface alloy*, Phys. Rev. Mater. **5**, 053403 (2021).
- [16] J. Yuhara, Y. Fujii, K. Nishino, N. Isobe, M. Nakatake, L. Xian, A. Rubio, and G. L. Lay, *Large area planar stanene epitaxially grown on Ag(111)*, 2D Mater. **5**, 025002 (2018).
- [17] M. H. Oliveira, J. M. J. Lopes, T. Schumann, L. A. Galves, M. Ramsteiner, K. Berlin, A. Trampert, and H. Riechert, *Synthesis of quasi-free-standing bilayer graphene nanoribbons on SiC surfaces*, Nat. Commun. **6**, 7632 (2015).
- [18] F. Mesple, N. R. Walet, G. Trambly de Laissardière, F. Guinea, D. Došenović, H. Okuno, C. Paillet, A. Michon, C. Chapelier, and V. T. Renard, *Giant Atomic Swirl in Graphene Bilayers with Biaxial Heterostrain*, Adv. Mater. **35**, 2306312 (2023).
- [19] Y. Du, J. Zhuang, J. Wang, Z. Li, H. Liu, J. Zhao, X. Xu, H. Feng, L. Chen, K. Wu, X. Wang, and S. X. Dou, *Quasi-freestanding epitaxial silicene on Ag(111) by oxygen intercalation*, Sci. Adv. **2**, e1600067 (2016).
- [20] Y. L. Chen, J. G. Analytis, J.-H. Chu, Z. K. Liu, S.-K. Mo, X. L. Qi, H. J. Zhang, D. H. Lu, X. Dai, Z. Fang, S. C. Zhang, I. R. Fisher, Z. Hussain, and Z.-X. Shen, *Experimental Realization of a Three-Dimensional Topological Insulator, Bi₂Te₃*, Science **325**, 178 (2009).
- [21] H. Zhang, C.-X. Liu, X.-L. Qi, X. Dai, Z. Fang, and S.-C. Zhang, *Topological insulators in Bi₂Se₃, Bi₂Te₃ and Sb₂Te₃ with a single Dirac cone on the surface*, Nat. Phys. **5**, 438 (2009).
- [22] B. Poudel, Q. Hao, Y. Ma, Y. Lan, A. Minnich, B. Yu, X. Yan, D. Wang, A. Muto, D. Vashaee, X. Chen, J. Liu, M. S. Dresselhaus, G. Chen, and Z. Ren, *High-Thermoelectric Performance of Nanostructured Bismuth Antimony Telluride Bulk Alloys*, Science **320**, 634 (2008).
- [23] S. Sarkar, J. Bhattacharya, P. Sadhukhan, D. Curcio, R. Dutt, V. K. Singh, M. Bianchi, A. Pariari, S. Roy, P. Mandal, T. Das, P. Hofmann, A. Chakrabarti, and S. R. Barman, *Charge density wave induced nodal lines in LaTe₃*, Nat. Commun. **14**, 3628 (2023).
- [24] M. N. Ali, J. Xiong, S. Flynn, J. Tao, Q. D. Gibson, L. M. Schoop, T. Liang, N. Haldolaarachchige, M. Hirschberger, N. P. Ong, and R. J. Cava, *Large, non-saturating magnetoresistance in WTe₂*, Nature **514**, 205 (2014).
- [25] A. Aharon-Steinberg, T. Völkl, A. Kaplan, A. K. Pariari, I. Roy, T. Holder, Y. Wolf, A. Y. Meltzer, Y. Myasoedov, M. E. Huber, B. Yan, G. Falkovich, L. S. Levitov, M. Hücker, and E. Zeldov, *Direct observation of vortices in an electron fluid*, Nature **607**, 74 (2022).
- [26] D. Kang, Y. Zhou, W. Yi, C. Yang, J. Guo, Y. Shi, S. Zhang, Z. Wang, C. Zhang, S. Jiang, A. Li, K. Yang, Q. Wu, G. Zhang, L. Sun, and Z. Zhao, *Superconductivity emerging from a suppressed large*

- magneto-resistant state in tungsten ditelluride*, Nat. Commun. **6**, 7804 (2015).
- [27] Z. Wang, B. J. Wieder, J. Li, B. Yan, and B. A. Bernevig, *Higher-Order Topology, Monopole Nodal Lines, and the Origin of Large Fermi Arcs in Transition Metal Dichalcogenides*, Phys. Rev. Lett. **123**, 186401 (2019).
- [28] M. M. Otrokov, I. I. Klimovskikh, H. Bentmann, D. Estyunin, A. Zeugner, Z. S. Aliev, S. Gaß, A. U. B. Wolter, A. V. Koroleva, A. M. Shikin, M. Blanco-Rey, M. Hoffmann, I. P. Rusinov, A. Y. Vyazovskaya, S. V. Eremeev, Y. M. Koroteev, V. M. Kuznetsov, F. Freyse, J. Sánchez-Barriga, I. R. Amiraslanov, M. B. Babanly, N. T. Mamedov, N. A. Abdullayev, V. N. Zverev, A. Alfonsov, V. Kataev, B. Büchner, E. F. Schwier, S. Kumar, A. Kimura, L. Petaccia, G. Di Santo, R. C. Vidal, S. Schatz, K. Kißner, M. Ünzelmann, C. H. Min, S. Moser, T. R. F. Peixoto, F. Reinert, A. Ernst, P. M. Echenique, A. Isaeva, and E. V. Chulkov, *Prediction and observation of an antiferromagnetic topological insulator*, Nature **576**, 416 (2019).
- [29] J. Li, Y. Li, S. Du, Z. Wang, B.-L. Gu, S.-C. Zhang, K. He, W. Duan, and Y. Xu, *Intrinsic magnetic topological insulators in van der Waals layered MnBi₂Te₄-family materials*, Sci. Adv. **5**, eaaw5685 (2019).
- [30] H. Padmanabhan, V. A. Stoica, P. K. Kim, M. Poore, T. Yang, X. Shen, A. H. Reid, M.-F. Lin, S. Park, J. Yang, H. H. Wang, N. Z. Koocher, D. Puggioni, A. B. Georgescu, L. Min, S. H. Lee, Z. Mao, J. M. Rondinelli, A. M. Lindenberg, L.-Q. Chen, X. Wang, R. D. Averitt, J. W. Freeland, and V. Gopalan, *Large Exchange Coupling Between Localized Spins and Topological Bands in MnBi₂Te₄*, Adv. Mater. **34**, 2202841 (2022).
- [31] A. Gao, Y.-F. Liu, J.-X. Qiu, B. Ghosh, T. V. Trevisan, Y. Onishi, C. Hu, T. Qian, H.-J. Tien, S.-W. Chen, M. Huang, D. Bérubé, H. Li, C. Tzschaschel, T. Dinh, Z. Sun, S.-C. Ho, S.-W. Lien, B. Singh, K. Watanabe, T. Taniguchi, D. C. Bell, H. Lin, T.-R. Chang, C. R. Du, A. Bansil, L. Fu, N. Ni, P. P. Orth, Q. Ma, and S.-Y. Xu, *Quantum metric nonlinear Hall effect in a topological antiferromagnetic heterostructure*, Science **381**, 181 (2023).
- [32] Y. J. Chen, L. X. Xu, J. H. Li, Y. W. Li, H. Y. Wang, C. F. Zhang, H. Li, Y. Wu, A. J. Liang, C. Chen, S. W. Jung, C. Cacho, Y. H. Mao, S. Liu, M. X. Wang, Y. F. Guo, Y. Xu, Z. K. Liu, L. X. Yang, and Y. L. Chen, *Topological Electronic Structure and Its Temperature Evolution in Antiferromagnetic Topological Insulator MnBi₂Te₄*, Phys. Rev. X **9**, 041040 (2019).
- [33] H. Li, S.-Y. Gao, S.-F. Duan, Y.-F. Xu, K.-J. Zhu, S.-J. Tian, J.-C. Gao, W.-H. Fan, Z.-C. Rao, J.-R. Huang, J.-J. Li, D.-Y. Yan, Z.-T. Liu, W.-L. Liu, Y.-B. Huang, Y.-L. Li, Y. Liu, G.-B. Zhang, P. Zhang,

- T. Kondo, S. Shin, H.-C. Lei, Y.-G. Shi, W.-T. Zhang, H.-M. Weng, T. Qian, and H. Ding, *Dirac Surface States in Intrinsic Magnetic Topological Insulators EuSn_2As_2 and $\text{MnBi}_{2n}\text{Te}_{3n+1}$* , Phys. Rev. X **9**, 041039 (2019).
- [34] B. Chen, F. Fei, D. Zhang, B. Zhang, W. Liu, S. Zhang, P. Wang, B. Wei, Y. Zhang, Z. Zuo, J. Guo, Q. Liu, Z. Wang, X. Wu, J. Zong, X. Xie, W. Chen, Z. Sun, S. Wang, Y. Zhang, M. Zhang, X. Wang, F. Song, H. Zhang, D. Shen, and B. Wang, *Intrinsic magnetic topological insulator phases in the Sb doped MnBi_2Te_4 bulks and thin flakes*, Nat. Commun. **10**, 4469 (2019).
- [35] X.-M. Ma, Y. Zhao, K. Zhang, S. Kumar, R. Lu, J. Li, Q. Yao, J. Shao, F. Hou, X. Wu, M. Zeng, Y.-J. Hao, Z. Hao, Y. Wang, X.-R. Liu, H. Shen, H. Sun, J. Mei, K. Miyamoto, T. Okuda, M. Arita, E. F. Schwier, K. Shimada, K. Deng, C. Liu, J. Lin, Y. Zhao, C. Chen, Q. Liu, and C. Liu, *Realization of a tunable surface Dirac gap in Sb-doped MnBi_2Te_4* , Phys. Rev. B **103**, L121112 (2021).
- [36] D. A. Glazkova, D. A. Estyunin, I. I. Klimovskikh, T. P. Makarova, O. E. Tereshchenko, K. A. Kokh, V. A. Golyashov, A. V. Koroleva, and A. M. Shikin, *Electronic Structure of Magnetic Topological Insulators $\text{Mn}(\text{Bi}_{1-x}\text{Sb}_x)_2\text{Te}_4$ with Various Concentration of Sb Atoms*, JETP Letters **115**, 286 (2022).
- [37] C.-C. Liu, W. Feng, and Y. Yao, *Quantum Spin Hall Effect in Silicene and Two-Dimensional Germanium*, Phys. Rev. Lett. **107**, 076802 (2011).
- [38] C. Kamal, A. Chakrabarti, and M. Ezawa, *Aluminene as highly hole-doped graphene*, New J. Phys. **17**, 083014 (2015).
- [39] D. Pesin and A. H. MacDonald, *Spintronics and pseudospintronics in graphene and topological insulators*, Nat. Mater. **11**, 409 (2012).
- [40] A. Molle, *Xenes: A New Emerging Two-Dimensional Materials Platform for Nanoelectronics*, ECS Trans. **75**, 163 (2016).
- [41] M. Wang, Y. Hu, J. Pu, Y. Zi, and W. Huang, *Emerging Xene-based Single-Atom Catalysts: Theory, Synthesis and Catalytic Applications*, Adv. Mater. **36**, 2303492 (2023).
- [42] W. Tao, N. Kong, X. Ji, Y. Zhang, A. Sharma, J. Ouyang, B. Qi, J. Wang, N. Xie, C. Kang, H. Zhang, O. C. Farokhzad, and J. S. Kim, *Emerging two-dimensional monoelemental materials (Xenes) for biomedical applications*, Chem. Soc. Rev. **48**, 2891 (2019).
- [43] C.-Z. Xu, Y.-H. Chan, Y. Chen, P. Chen, X. Wang, C. Dejoie, M.-H. Wong, J. A. Hlevyack, H. Ryu, H.-Y. Kee, N. Tamura, M.-Y. Chou, Z. Hussain, S.-K. Mo, and T.-C. Chiang, *Elemental Topological Dirac Semimetal: α -Sn on $\text{InSb}(111)$* , Phys. Rev. Lett. **118**, 146402 (2017).
- [44] J. Li, T. Lei, J. Wang, R. Wu, J. Zhao, L. Zhao, Y. Guo, H. Qian, and K. Ibrahim, *Anisotropic Electronic*

- Structure and Interfacial Chemical Reaction of Stanene/Bi₂Te₃*, J. Phys. Chem. C **124**, 4917 (2020).
- [45] X. Zheng, J.-F. Zhang, B. Tong, and R.-R. Du, *Epitaxial growth and electronic properties of few-layer stanene on InSb (111)*, 2D Mater. **7**, 011001 (2019).
- [46] J. Gou, L. Kong, H. Li, Q. Zhong, W. Li, P. Cheng, L. Chen, and K. Wu, *Strain-induced band engineering in monolayer stanene on Sb(111)*, Phys. Rev. Mater. **1**, 054004 (2017).
- [47] P. Sadhukhan, D. Pandey, V. K. Singh, S. Sarkar, A. Rai, K. Bhattacharya, A. Chakrabarti, and S. R. Barman, *Electronic structure and morphology of thin surface alloy layers formed by deposition of Sn on Au(111)*, Appl. Surf. Sci. **506**, 144606 (2020).
- [48] J. Shah, W. Wang, H. M. Sohail, and R. I. G. Uhrberg, *Atomic and electronic structures of the surface alloy on Au(111)*, Phys. Rev. B **104**, 125408 (2021).
- [49] P. Sadhukhan, S. Barman, T. Roy, V. K. Singh, S. Sarkar, A. Chakrabarti, and S. R. Barman, *Electronic structure of Au-Sn compounds grown on Au(111)*, Phys. Rev. B **100**, 235404 (2019).
- [50] Y. Deng, Y. Yu, M. Z. Shi, Z. Guo, Z. Xu, J. Wang, X. H. Chen, and Y. Zhang, *Quantum anomalous Hall effect in intrinsic magnetic topological insulator MnBi₂Te₄*, Science **367**, 895 (2020).
- [51] F. D. M. Haldane, *Model for a Quantum Hall Effect without Landau Levels: Condensed-Matter Realization of the “Parity Anomaly”*, Phys. Rev. Lett. **61**, 2015 (1988).
- [52] R. Yu, W. Zhang, H.-J. Zhang, S.-C. Zhang, X. Dai, and Z. Fang, *Quantized Anomalous Hall Effect in Magnetic Topological Insulators*, Science **329**, 61 (2010).
- [53] J. Zhang, C.-Z. Chang, P. Tang, Z. Zhang, X. Feng, K. Li, L. li Wang, X. Chen, C. Liu, W. Duan, K. He, Q.-K. Xue, X. Ma, and Y. Wang, *Topology-Driven Magnetic Quantum Phase Transition in Topological Insulators*, Science **339**, 1582 (2013).
- [54] C. Biswas, A. K. Shukla, S. Banik, S. R. Barman, and A. Chakrabarti, *Argon Nanobubbles in Al(111): A Photoemission Study*, Phys. Rev. Lett. **92**, 115506 (2004).
- [55] S. Tougaard, *Practical algorithm for background subtraction*, Surf. Sci. **216**, 343 (1989).
- [56] D. Nečas and P. Klapetek, *Gwyddion: an open-source software for SPM data analysis*, Open Phys. **10**, 181–188 (2011).
- [57] G. Kresse and D. Joubert, *From ultrasoft pseudopotentials to the projector augmented-wave method*, Phys. Rev. B **59**, 1758 (1999).
- [58] J. P. Perdew, K. Burke, and M. Ernzerhof, *Generalized Gradient Approximation Made Simple*, Phys. Rev. Lett. **77**, 3865 (1996).
- [59] G. Kresse and J. Furthmüller, *Efficient iterative schemes for ab initio total-energy calculations using*

- a plane-wave basis set*, Phys. Rev. B **54**, 11169 (1996).
- [60] H. J. Monkhorst and J. D. Pack, *Special points for Brillouin-zone integrations*, Phys. Rev. B **13**, 5188 (1976).
- [61] K. Momma and F. Izumi, *VESTA 3 for three-dimensional visualization of crystal, volumetric and morphology data*, J. Appl. Crystallogr. **44**, 1272 (2011).
- [62] A. K. Shukla, S. Banik, R. S. Dhaka, C. Biswas, S. R. Barman, and H. Haak, *Versatile UHV compatible Knudsen type effusion cell*, Rev. Sci. Instrum. **75**, 4467 (2004).
- [63] S. H. Lee, D. Graf, L. Min, Y. Zhu, H. Yi, S. Ciocys, Y. Wang, E. S. Choi, R. Basnet, A. Fereidouni, A. Wegner, Y.-F. Zhao, K. Verlinde, J. He, R. Redwing, V. Gopalan, H. O. H. Churchill, A. Lanzara, N. Samarth, C.-Z. Chang, J. Hu, and Z. Q. Mao, *Evidence for a Magnetic-Field-Induced Ideal type-II Weyl State in Antiferromagnetic Topological Insulator $Mn(Bi_{1-x}Sb_x)_2Te_4$* , Phys. Rev. X **11**, 031032 (2021).
- [64] J. Nayak, M. Maniraj, A. Rai, S. Singh, P. Rajput, A. Gloskovskii, J. Zegenhagen, D. L. Schlagel, T. A. Lograsso, K. Horn, and S. R. Barman, *Bulk Electronic Structure of Quasicrystals*, Phys. Rev. Lett. **109**, 216403 (2012).
- [65] S. Tanuma, C. J. Powell, and D. R. Penn, *Calculations of electron inelastic mean free paths. IX. Data for 41 elemental solids over the 50 eV to 30 keV range*, Surf. Interface Anal. **43**, 689 (2011).
- [66] See Supplementary Material at <http://> for Figs. S1-S29, Tables S I-S IV.
- [67] M. Trzhaskovskaya and V. Yarzhemsky, *Dirac–Fock photoionization parameters for HAXPES applications*, At. Data Nucl. Data Tables **119**, 99 (2018).
- [68] K. Voleckaert, P. Majchrzak, D. Biswas, A. J. H. Jones, M. Bianchi, Z. Jiang, R. Dubourg, R. Stenshoj, M. L. Jensen, N. C. Jones, S. V. Hoffmann, J.-L. Mi, M. Bremholm, X.-C. Pan, Y. P. Chen, P. Hoffmann, J. A. Miwa, and S. Ulstrup, *Surface Electronic Structure Engineering of Manganese Bismuth Tellurides Guided by Micro-Focused Angle-Resolved Photoemission*, Adv. Mater. **35**, 2301907 (2023).
- [69] R. B. Shalvoy, G. B. Fisher, and P. J. Stiles, *Bond ionicity and structural stability of some average-valence-five materials studied by x-ray photoemission*, Phys. Rev. B **15**, 1680 (1977).
- [70] J. B. Mann, T. L. Meek, and L. C. Allen, *Configuration Energies of the Main Group Elements*, J. Am. Chem. Soc. **122**, 2780 (2000).
- [71] J. A. Leiro, M. H. Heinonen, S. Mattila, and A. Szczerbakow, *Surface core-level shifts in $CdTe_{1-x}S_x(110)$ and $CdTe_{1-x}Se_x(110)$* , Phys. Rev. B **73**, 205323 (2006).
- [72] K. Prince, G. Paolucci, V. Cháb, M. Surman, and A. Bradshaw, *Surface core level shifts of A II–VI*

- compound: CdTe*, Surf. Sci. **206**, L871 (1988).
- [73] V. K. Singh, M. Mihalkovič, M. Krajčí, S. Sarkar, P. Sadhukhan, M. Maniraj, A. Rai, K. Pussi, D. L. Schlagel, T. A. Lograsso, A. K. Shukla, and S. R. Barman, *Quasiperiodic ordering in thick Sn layer on i-Al-Pd-Mn: A possible quasicrystalline clathrate*, Phys. Rev. Res. **2**, 013023 (2020).
- [74] B. Cordero, V. Gómez, A. E. Platero-Prats, M. Revés, J. Echeverría, E. Cremades, F. Barragán, and S. Alvarez, *Covalent radii revisited*, Dalton Trans. , 2832 (2008).
- [75] J.-Q. Yan, S. Okamoto, M. A. McGuire, A. F. May, R. J. McQueeney, and B. C. Sales, *Evolution of structural, magnetic, and transport properties in $MnBi_{2-x}Sb_xTe_4$* , Phys. Rev. B **100**, 104409 (2019).
- [76] Y.-H. Song, Z.-W. Wang, Z.-Y. Jia, X.-Y. Zhu, Z.-Q. Shi, L. Zhu, Q.-Q. Yuan, D.-J. Shu, and S.-C. Li, *High-buckled stanene with a topologically nontrivial energy gap*, J. Phys. D: Appl. Phys. **54**, 304002 (2021).
- [77] M.-X. Wang, P. Li, J.-P. Xu, Z.-L. Liu, J.-F. Ge, G.-Y. Wang, X. Yang, Z.-A. Xu, S.-H. Ji, C. L. Gao, D. Qian, W. Luo, C. Liu, and J.-F. Jia, *Interface structure of a topological insulator/superconductor heterostructure*, New J. Phys. **16**, 123043 (2014).
- [78] H. Yi, L.-H. Hu, Y. Wang, R. Xiao, J. Cai, D. R. Hickey, C. Dong, Y.-F. Zhao, L.-J. Zhou, R. Zhang, A. R. Richardella, N. Alem, J. A. Robinson, M. H. W. Chan, X. Xu, N. Samarth, C.-X. Liu, and C.-Z. Chang, *Crossover from Ising- to Rashba-type superconductivity in epitaxial Bi_2Se_3 /monolayer $NbSe_2$ heterostructures*, Nat. Mater. **21**, 1366 (2022).
- [79] A. Janzen, I. Dumkow, and M. H. von Hoegen, *Thermal activation of dislocation array formation*, Appl. Phys. Lett. **79**, 2387 (2001).
- [80] V. Zielasek, T. Hildebrandt, and M. Henzler, *Surface color centers on epitaxial NaCl films*, Phys. Rev. B **62**, 2912 (2000).
- [81] M. Garnica, M. M. Otrokov, P. C. Aguilar, I. I. Klimovskikh, D. Estyunin, Z. S. Aliev, I. R. Amiraslanov, N. A. Abdullayev, V. N. Zverev, M. B. Babanly, N. T. Mamedov, A. M. Shikin, A. Arnau, A. L. V. de Parga, E. V. Chulkov, and R. Miranda, *Native point defects and their implications for the Dirac point gap at $MnBi_2Te_4$ (0001)*, npj Quantum Mater. **7**, 7 (2022).
- [82] F. Lüpke, M. Kolmer, J. Yan, H. Chang, P. Vilmercati, H. H. Weitering, W. Ko, and A.-P. Li, *Anti-site defect-induced disorder in compensated topological magnet $MnBi_{2-x}Sb_xTe_4$* , Commun. Mater. **4**, 82 (2023).
- [83] M. Neupane, S.-Y. Xu, L. A. Wray, A. Petersen, R. Shankar, N. Alidoust, C. Liu, A. Fedorov, H. Ji, J. M. Allred, Y. S. Hor, T.-R. Chang, H.-T. Jeng, H. Lin, A. Bansil, R. J. Cava, and M. Z. Hasan,

- Topological surface states and Dirac point tuning in ternary topological insulators*, Phys. Rev. B **85**, 235406 (2012).
- [84] J. Li, T. Lei, J. Wang, R. Wu, H. Qian, and K. Ibrahim, *In-plane crystal field constrained electronic structure of stanene*, Appl. Phys. Lett. **116**, 101601 (2020).
- [85] P. Redhead, in *AIP Conf. Proc.* (2003) pp. 243–254.
- [86] S. Avdiaj and B. Erjavec, *Outgassing of hydrogen from a stainless steel vacuum chamber*, Mater. Tehnol **46**, 161 (2012).
- [87] I. Lefebvre, M. A. Szymanski, J. Olivier-Fourcade, and J. C. Jumas, *Electronic structure of tin monochalcogenides from SnO to SnTe*, Phys. Rev. B **58**, 1896 (1998).
- [88] B. Liu, C. Xiao, Q. Zhu, J. Wu, Y. Cui, H. Wang, Z. Wang, Y. Lu, Z. Ren, and G.-h. Cao, *Superconducting phase diagram and nontrivial band topology of structurally modulated $\text{Sn}_{1-x}\text{Sb}_x$* , Phys. Rev. Mater. **3**, 084603 (2019).
- [89] A. S. Erickson, J.-H. Chu, M. F. Toney, T. H. Geballe, and I. R. Fisher, *Enhanced superconducting pairing interaction in indium-doped tin telluride*, Phys. Rev. B **79**, 024520 (2009).
- [90] MBT and higher n members of the series $\text{MnBi}_2\text{Te}_4(\text{Bi}_2\text{Te}_3)_n$ exhibit antiferromagnetic interaction between Mn layers up to $n=2$. So, the magnetic interaction range in this series is expected to be more than or equal to the Mn layer separation (3.36 nm for $n=2$) [91].
- [91] I. I. Klimovskikh, M. M. Otrokov, D. Estyunin, S. V. Eremeev, S. O. Filnov, A. Koroleva, E. Shevchenko, V. Voroshnin, A. G. Rybkin, I. P. Rusinov, M. Blanco-Rey, M. Hoffmann, Z. S. Aliev, M. B. Babanly, I. R. Amiraslanov, N. A. Abdullayev, V. N. Zverev, A. Kimura, O. E. Tereshchenko, K. A. Kokh, L. Petaccia, G. Di Santo, A. Ernst, P. M. Echenique, N. T. Mamedov, A. M. Shikin, and E. V. Chulkov, *Tunable 3D/2D magnetism in the $(\text{MnBi}_2\text{Te}_4)(\text{Bi}_2\text{Te}_3)_m$ topological insulators family*, npj Quantum Mater. **5**, 54 (2020).

Supplementary material for manuscript entitled
“Growth of bilayer stanene on a magnetic topological insulator aided by a
buffer layer”

Sajal Barman^{1,†}, Pramod Bhakuni^{1,†}, Shuvam Sarkar¹, Joydipto Bhattacharya^{2,3},
Mohammad Balal¹, Mrinal Manna¹, Soumen Giri¹, Arnab Kumar Pariari⁴, Tomáš Skála⁵,
Markus Hücker⁴, Rajib Batabyal¹, Aparna Chakrabarti^{2,3}, and Sudipta Roy Barman^{1*}

¹*UGC-DAE Consortium for Scientific Research,
Khandwa Road, Indore, 452001, India*

²*Theory and Simulations Laboratory, Raja Ramanna Centre for Advanced Technology,
Indore 452013, Madhya Pradesh, India*

³*Homi Bhabha National Institute, Training School Complex,
Anushakti Nagar, Mumbai 400094, Maharashtra, India*

⁴*Department of Condensed Matter Physics,
Weizmann Institute of Science, Rehovot, Israel and*

⁵*Charles University, Faculty of Mathematics and Physics,
V Holešovičkách 2, CZ-18000 Prague 8, Czech Republic.*

† Both authors contributed equally.

The Supplementary Material consists of twenty nine figures Fig. S 1 to Fig. S 29, four tables Table S I to Table S IV.

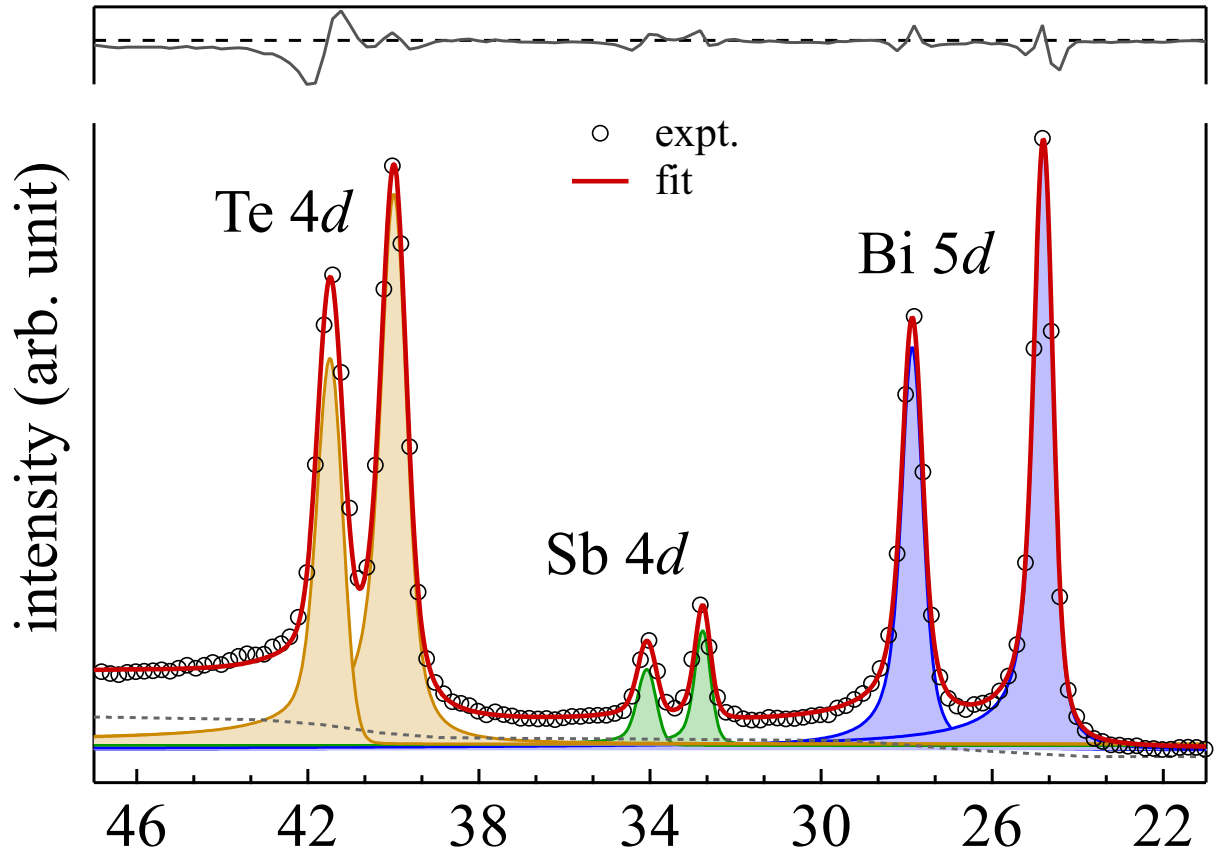


Fig. S 1. Bi 5*d*, Sb 4*d* and Te 4*d* HAXPES core level spectra (black open circles) of MBST measured with 6 keV photon energy. The fit (red curve) to the spectrum includes an inelastic background (black dashed curve). The residual of the fitting is shown in the top the panel. The Bi 5*d*, Sb 4*d*, and Te 4*d* core level peaks with spin-orbit splitting of 3.1, 1.3 and 1.5 eV are shown by blue, green and orange curves, respectively. A 30% Sb doping is obtained from the relative intensities of the peaks, as shown by the ratio of Bi:Sb:Te \approx 0.7:0.3:2.

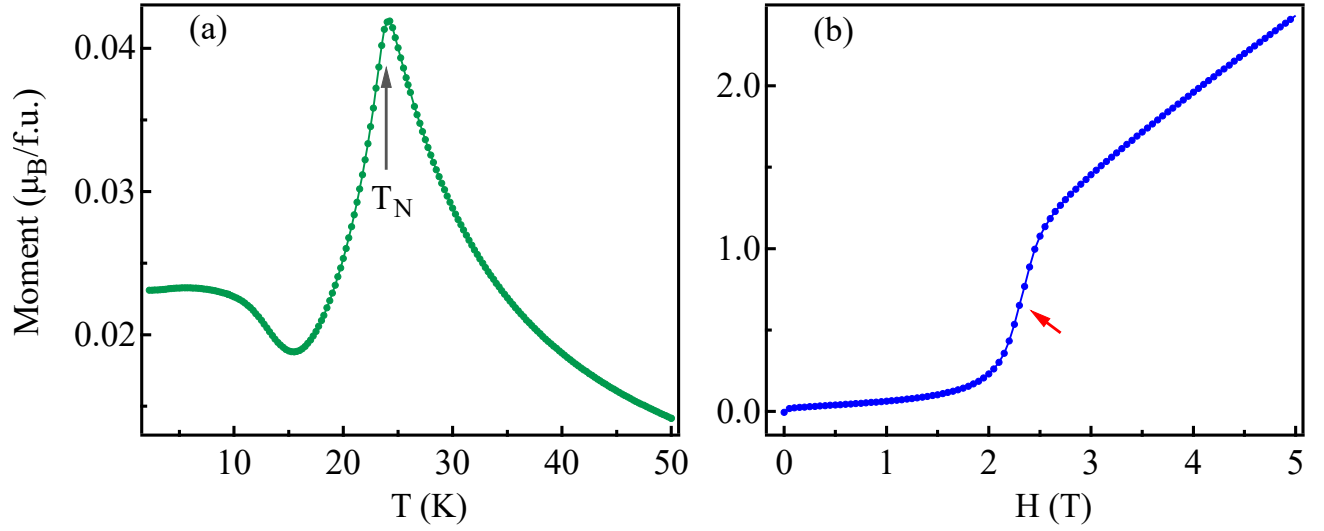


Fig. S 2. Magnetic characterization of MBST crystal with the magnetic field (H) parallel to the c -axis. (a) Magnetization (M) as a function of temperature at $H= 0.1$ Tesla, the gray arrow indicates the Neel temperature (T_N) to be 24 K. (b) $M(H)$ measurement at 2 K, the red arrow indicates the spin flop transition at 2.3 Tesla.

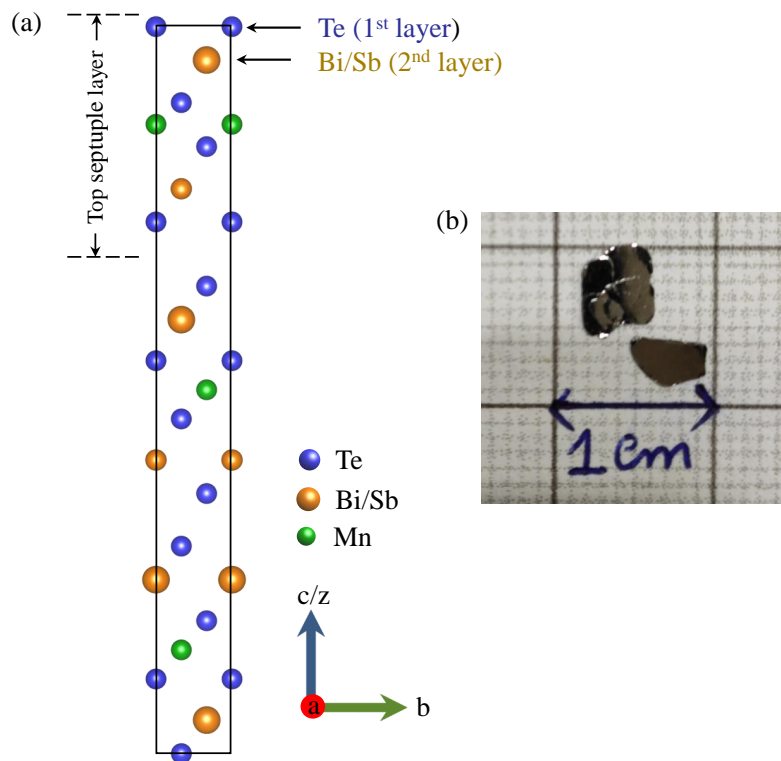


Fig. S 3. (a) The unit cell of $\text{Mn}(\text{Bi}_{0.7}\text{Sb}_{0.3})_2\text{Te}_4$ (MBST), where Te (Bi/Sb) constitutes top (second) layer of the (0001) surface. It has a $R\bar{3}m$ space group with lattice parameters $a = 0.43$ nm and $c = 4.092$ nm [1] consisting of three septuple layers that are coupled by van der Waals (vdW) interaction. (b) A photograph of the MBST crystals used in the present study.

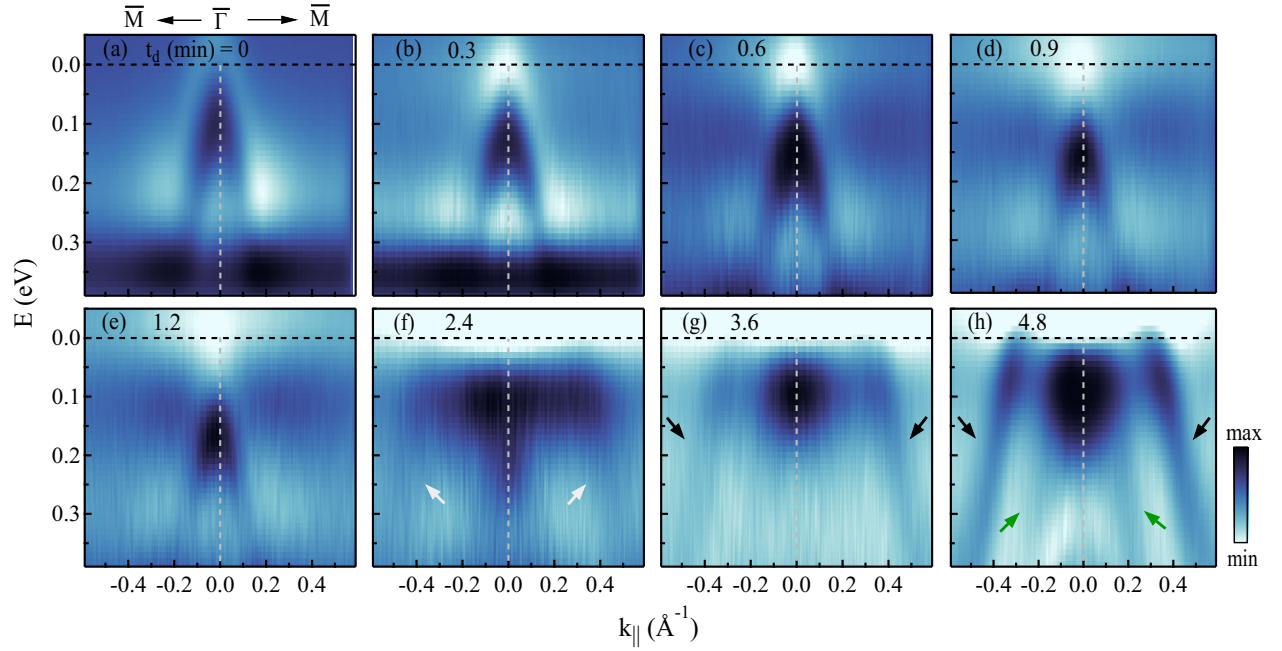


Fig. S 4. (a-h) The second derivative ARPES intensity plot towards $\bar{\Gamma}$ - \bar{M} direction corresponding to the raw data in Fig. 1 of the main manuscript. The black and green arrows highlight the outer and inner monolayer stanene bands, respectively. The white arrows in panel **f** indicate a BL related band. The color scale is shown on the right.

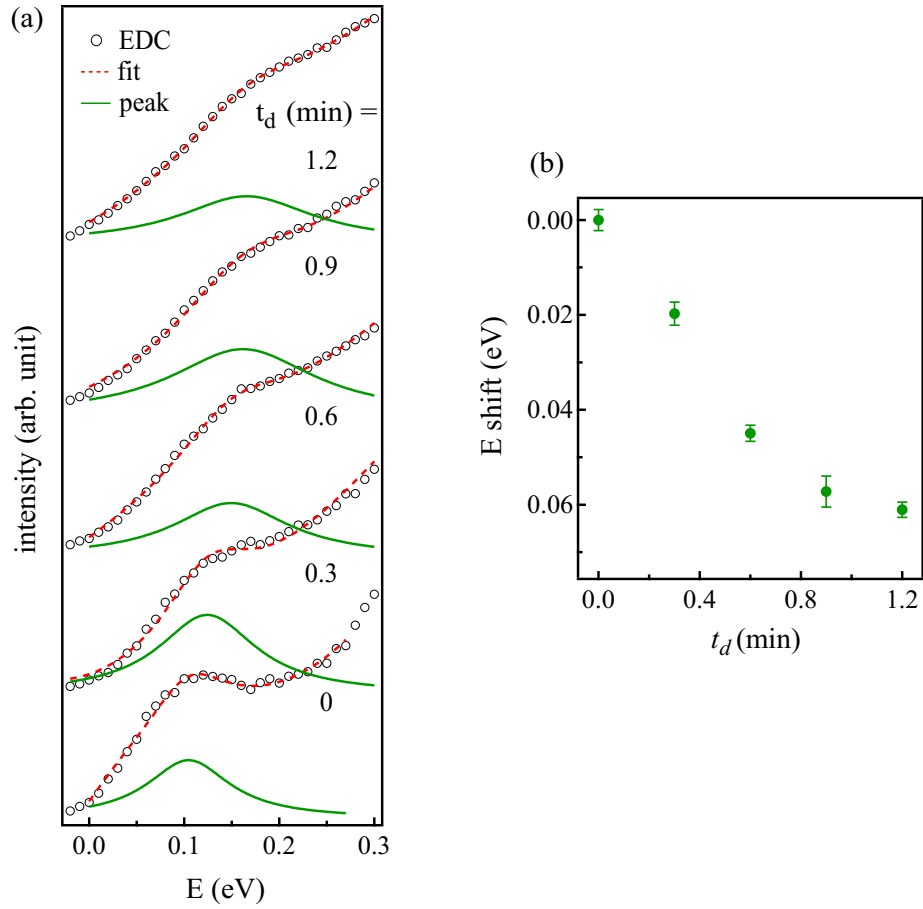


Fig. S 5. (a) The energy distribution curves (EDCs) of the raw ARPES spectra shown in Fig. 1 of the main text at $\bar{\Gamma}$ point, as a function of Sn deposition on MBST for different t_d . The maximum of the Lorentzian function (green curve) that has been used to fit the EDCs along with a linear background represents the band maximum. (b) The E shift in the band maxima from panels **a** as a function of t_d .

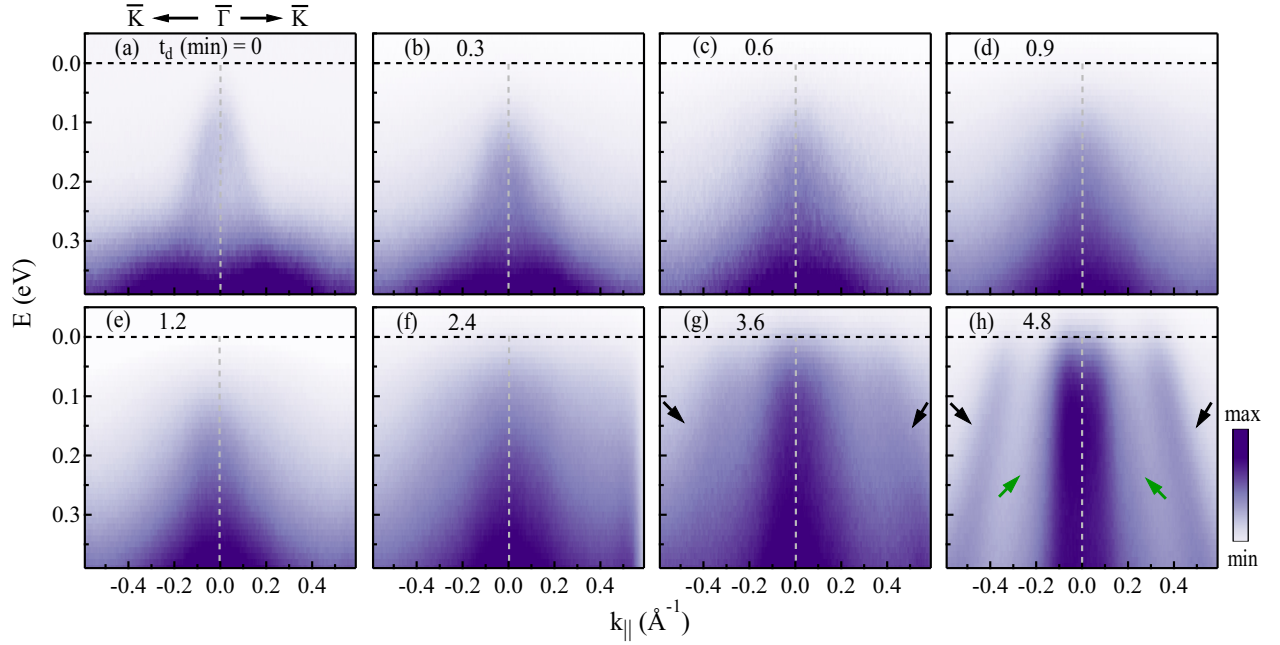


Fig. S 6. (a-h) The raw ARPES intensity plots towards $\bar{\Gamma}$ - \bar{K} for Sn deposition on MBST for different t_d . The black and green arrows highlight the outer and inner monolayer stanene bands, respectively. The color scale is shown on the right side.

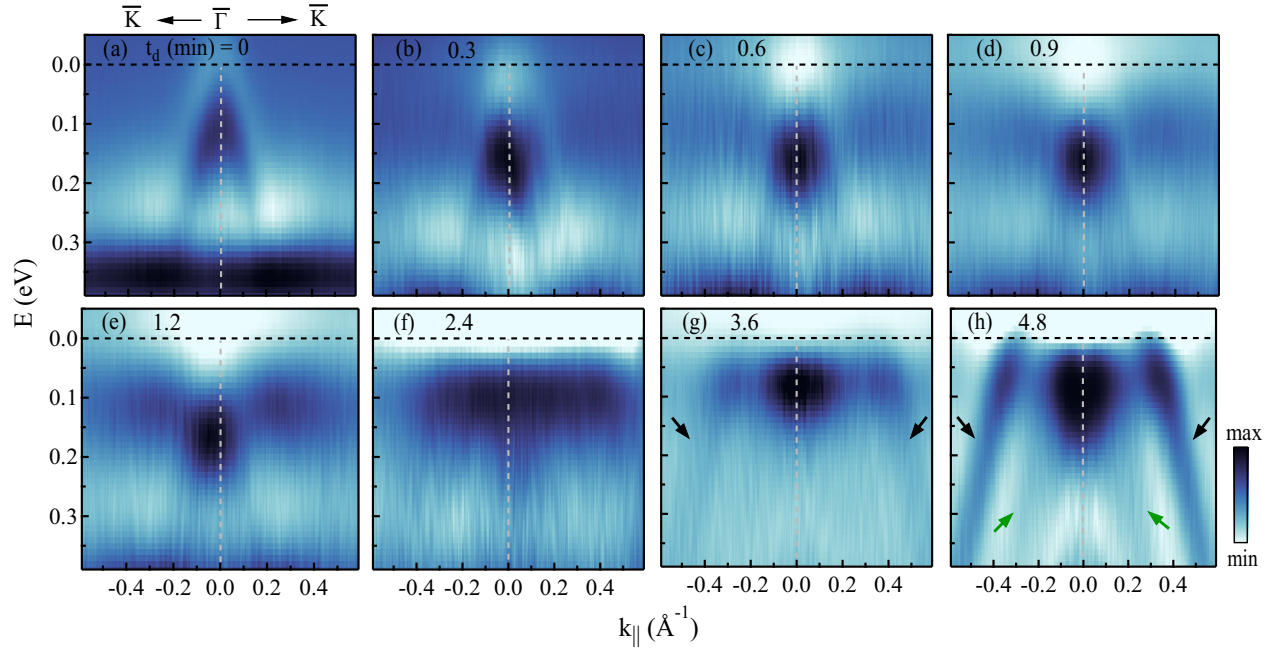


Fig. S 7. (a-h) The second derivative ARPES intensity plots towards $\bar{\Gamma}-\bar{K}$ for the raw data in Fig. S6 for Sn deposition on MBST for different t_d . The black and green arrows highlight the outer and inner monolayer stanene bands, respectively. The color scale is shown on the right side.

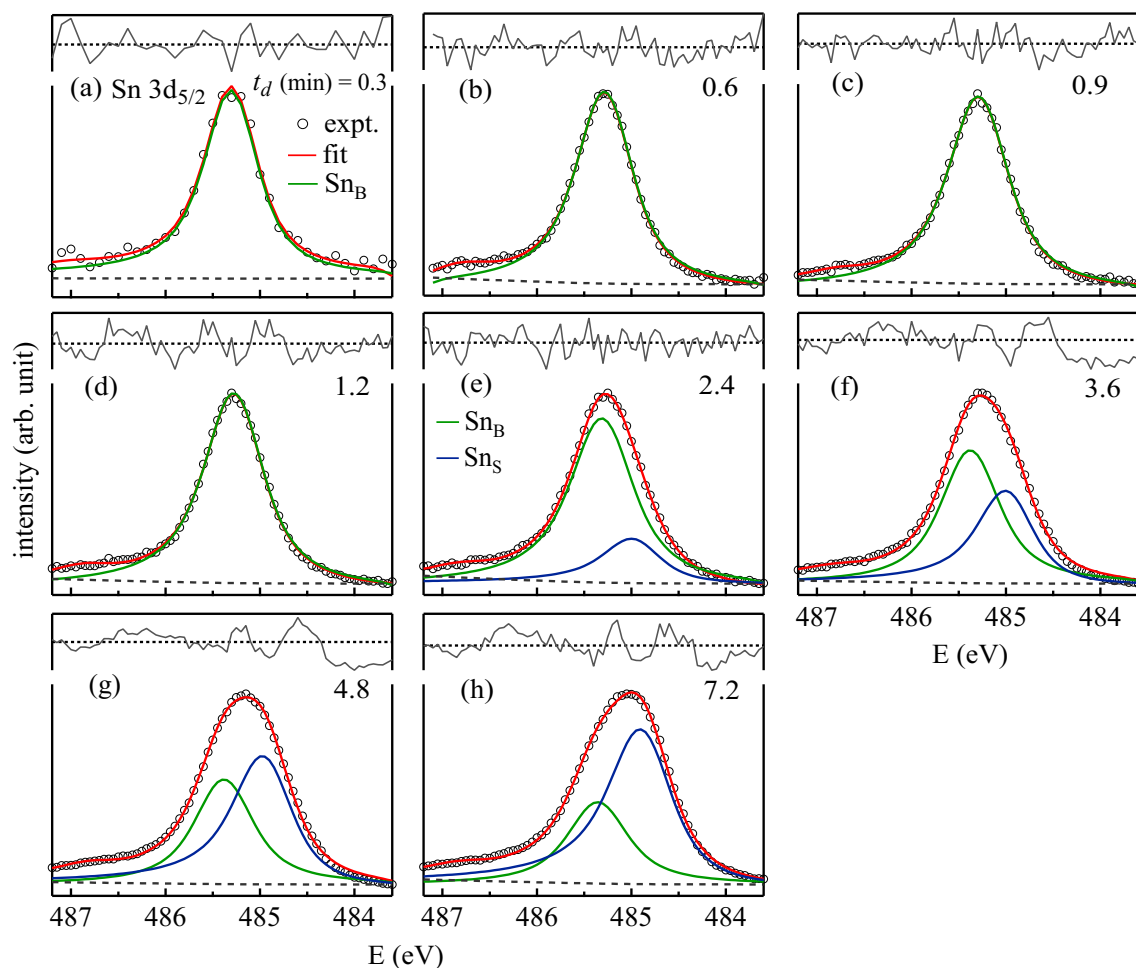


Fig. S 8. (a-h) Sn $3d_{5/2}$ XPS core level spectra at different Sn depositions are fitted by least square error minimization method. All the spectra are normalized to the same height. At the top of each panel, the residual of the fitting (gray curve) that exhibits random variation around zero (black dashed line) shows the good quality of the fit. An inelastic background that is included in the fitting is shown by black dashed curve.

Table S I. Parameters obtained from least square fitting of Sn $3d_{5/2}$ core level spectra, e.g., the binding energy (E), the life time broadening (2γ) of the components Sn_B, Sn_S and the goodness of fit (χ^2).

t_d (min)	$E \pm 0.025$ (eV)		$2\gamma \pm 0.05$ (eV)		χ^2
components	Sn _B	Sn _S	Sn _B	Sn _S	
0.3	485.29	-	0.49	-	0.033
0.6	485.27	-	0.55	-	0.009
0.9	485.28	-	0.60	-	0.012
1.2	485.27	-	0.60	-	0.011
2.4	485.30	484.97	0.65	0.56	0.006
3.6	485.38	484.97	0.60	0.55	0.013
4.8	485.38	484.94	0.60	0.60	0.014
7.2	485.36	484.87	0.60	0.67	0.007

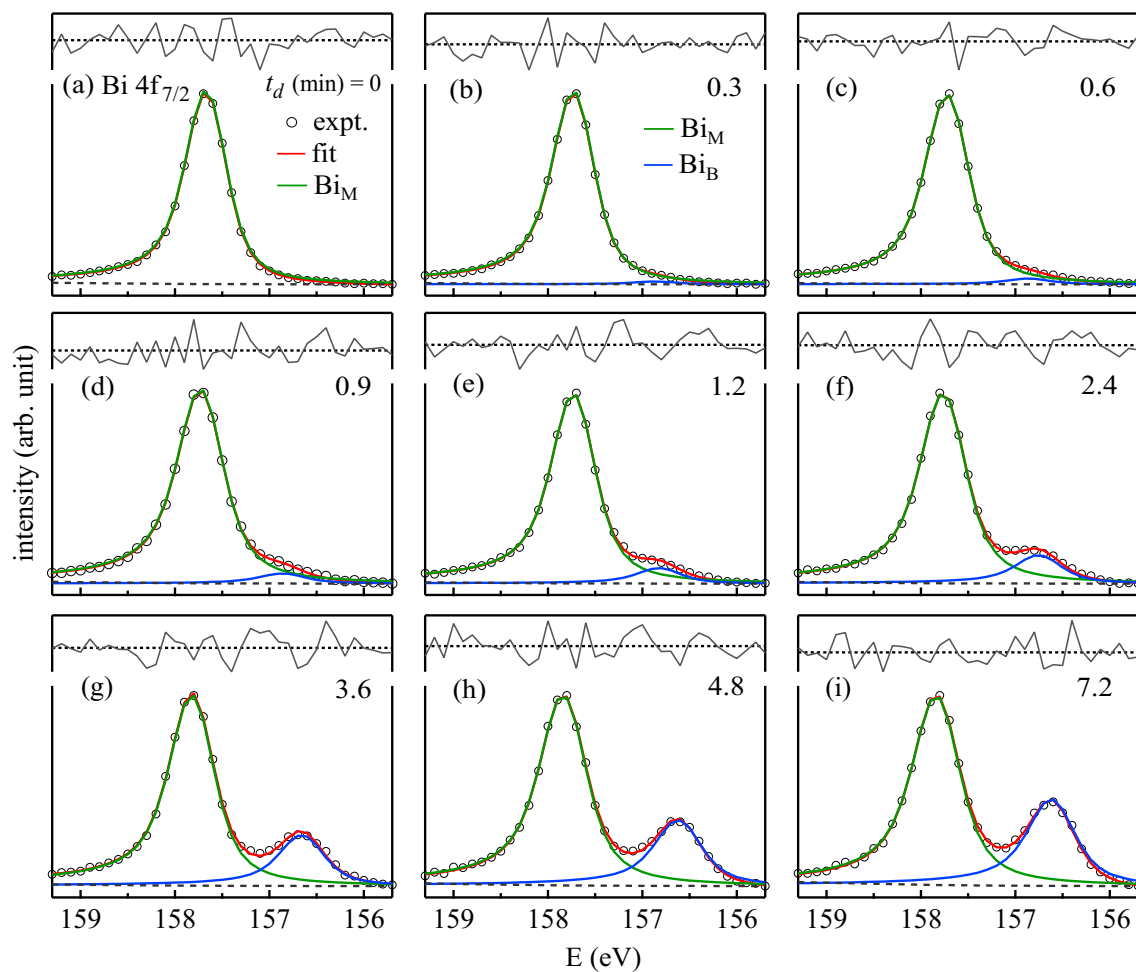


Fig. S 9. (a-i) Bi $4f_{7/2}$ XPS core level spectra at different Sn depositions are fitted by least square error minimization method. All the spectra are normalized to the same height. At the top of each panel, the residual of the fitting (gray curve) that exhibits random variation around zero (black dashed line) shows the good quality of the fit. An inelastic background that is included in the fitting is shown by black dashed curve.

Table S II. Parameters obtained from least square fitting of Bi $4f_{7/2}$ core level spectra, e.g., the binding energy (E), the life time broadening (2γ) of the components Bi_M, Bi_B and the goodness of fit (χ^2). 2γ was constrained to vary between 0.26 to 0.4 eV.

t_d (min)	$E \pm 0.025$ (eV)		$2\gamma \pm 0.05$ (eV)		χ^2
components	Bi _M	Bi _B	Bi _M	Bi _B	
0	157.65	-	0.28	-	0.005
0.3	157.71	156.85	0.29	0.29	0.005
0.6	157.71	156.85	0.32	0.32	0.008
0.9	157.71	156.85	0.37	0.37	0.003
1.2	157.72	156.80	0.33	0.33	0.003
2.4	157.75	156.74	0.36	0.36	0.004
3.6	157.80	156.64	0.34	0.34	0.005
4.8	157.82	156.60	0.38	0.38	0.004
7.2	157.82	156.60	0.39	0.39	0.003

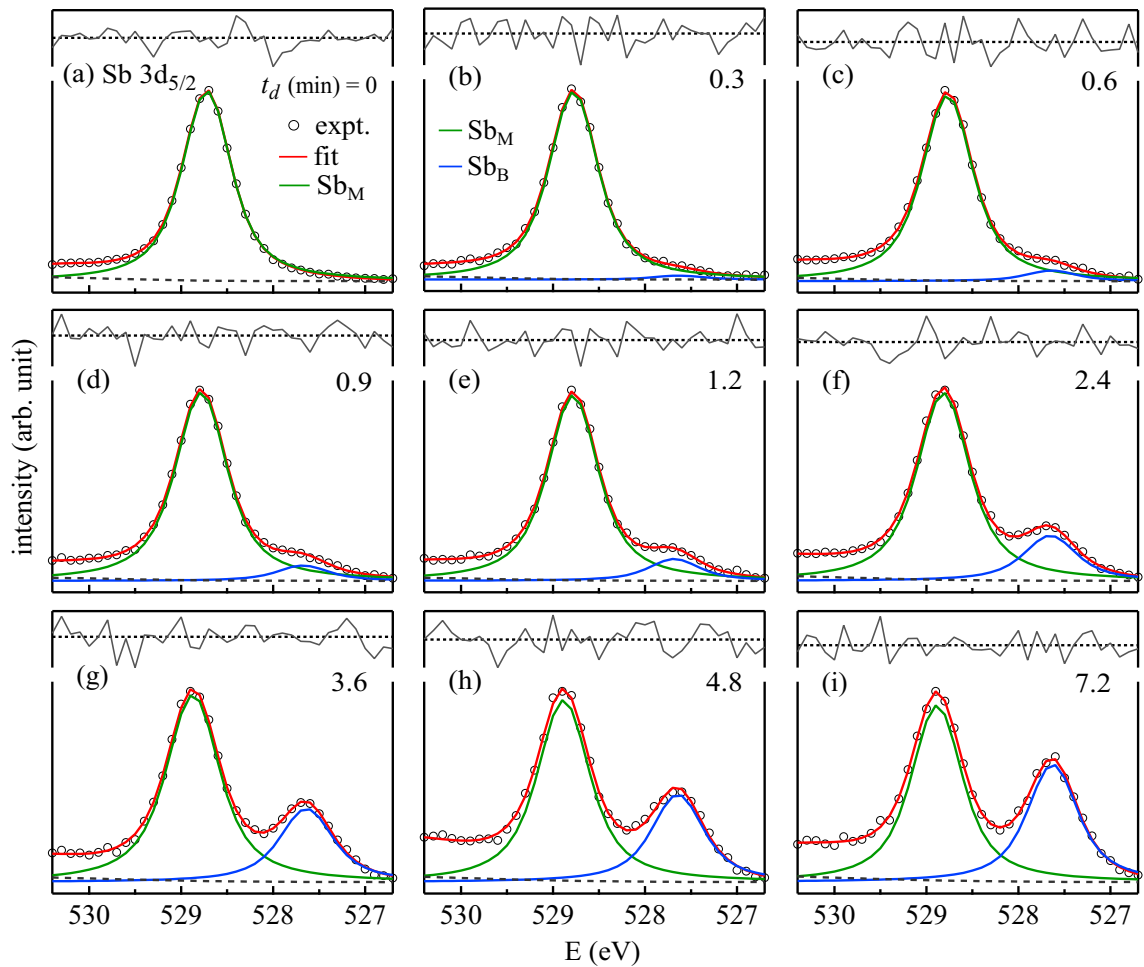


Fig. S 10. (a-i) Sb $3d_{5/2}$ XPS core level spectra at different Sn depositions are fitted by least square error minimization method. All the spectra are normalized to the same height. At the top of each panel, the residual of the fitting (gray curve) that exhibits random variation around zero (black dashed line) shows the good quality of the fit. An inelastic background that is included in the fitting is shown by black dashed curve.

Table S III. Parameters obtained from least square fitting of Sb $3d_{5/2}$ core level spectra, e.g., the binding energy (E), the life time broadening (2γ) of the components Sb_M , Sb_B and the goodness of fit (χ^2). 2γ was allowed to vary between 0.42 to 0.54 eV.

t_d (min)	$E \pm 0.025$ (eV)		$2\gamma \pm 0.05$ (eV)		χ^2
components	Sb_M	Sb_B	Sb_M	Sb_B	
0	528.72	-	0.46	-	0.002
0.3	528.77	527.64	0.46	0.46	0.004
0.6	528.77	527.64	0.48	0.48	0.002
0.9	528.78	527.68	0.50	0.50	0.004
1.2	528.79	527.68	0.48	0.48	0.004
2.4	528.81	527.66	0.52	0.52	0.006
3.6	528.87	527.64	0.53	0.53	0.007
4.8	528.88	527.64	0.51	0.51	0.013
7.2	528.89	527.63	0.50	0.50	0.014

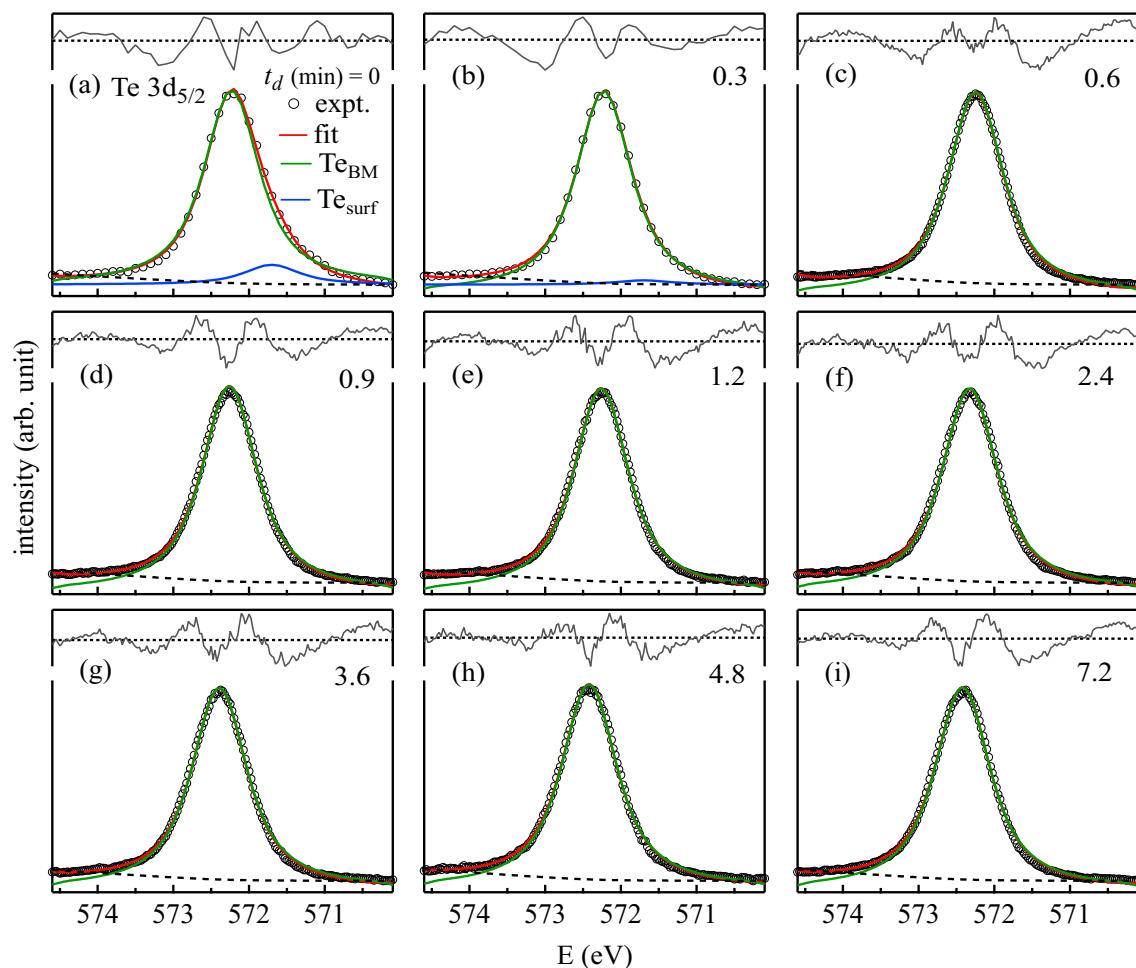


Fig. S 11. (a-i) Te $3d_{5/2}$ XPS core level spectra at different Sn depositions are fitted by least square error minimization method. All the spectra are normalized to the same height. At the top of each panel, the residual of the fitting (gray curve) that exhibits random variation around zero (black dashed line) shows the good quality of the fit. An inelastic background that is included in the fitting is shown by black dashed curve.

Table S IV. Parameters obtained from least square fitting of Te $3d_{5/2}$ core level spectra, e.g., the binding energy (E), the life time broadening (2γ) of the components Te_{BM} , Te_{surf} and the goodness of fit (χ^2).

t_d (min)	$E \pm 0.025$ (eV)		$2\gamma \pm 0.05$ (eV)		χ^2
components	Te_{BM}	Te_{surf}	Te_{BM}	Te_{surf}	
0	572.23	571.70	0.75	0.75	0.005
0.3	572.23	571.70	0.75	0.75	0.004
0.6	572.25	-	0.72	-	0.026
0.9	572.26	-	0.76	-	0.032
1.2	572.26	-	0.74	-	0.029
2.4	572.32	-	0.75	-	0.032
3.6	572.39	-	0.75	-	0.029
4.8	572.42	-	0.75	-	0.035
7.2	572.42	-	0.75	-	0.035

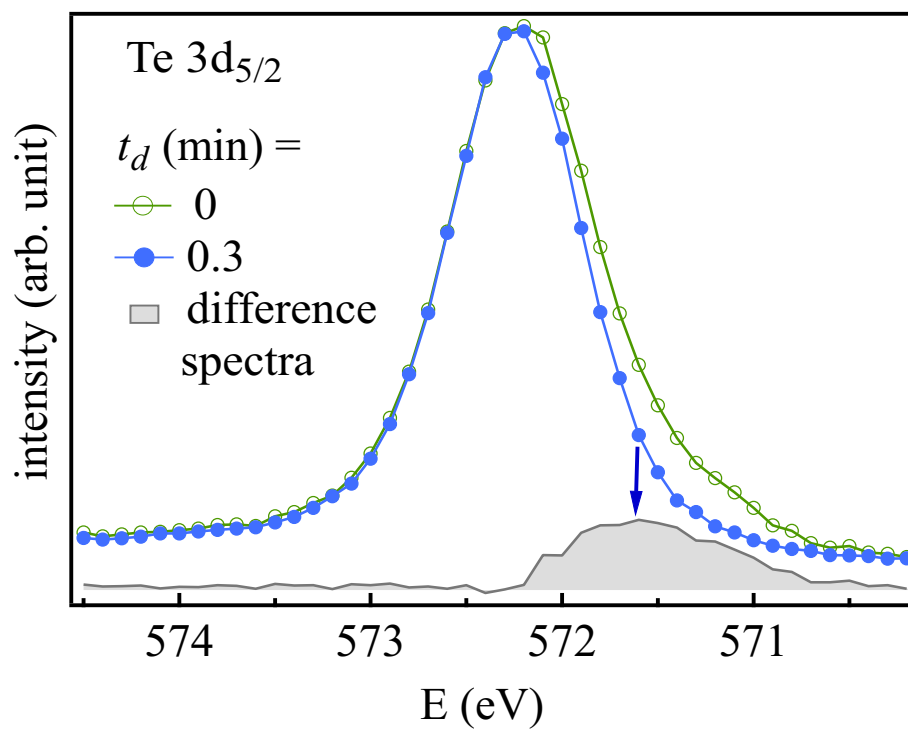


Fig. S 12. Te 3d_{5/2} core level spectra of MBST ($t_d = 0$) compared to that for Sn deposition of 0.3 min, both normalized to the same height. Their difference spectrum (gray shaded) represents the surface core level peak, the peak position is shown by a blue arrow.

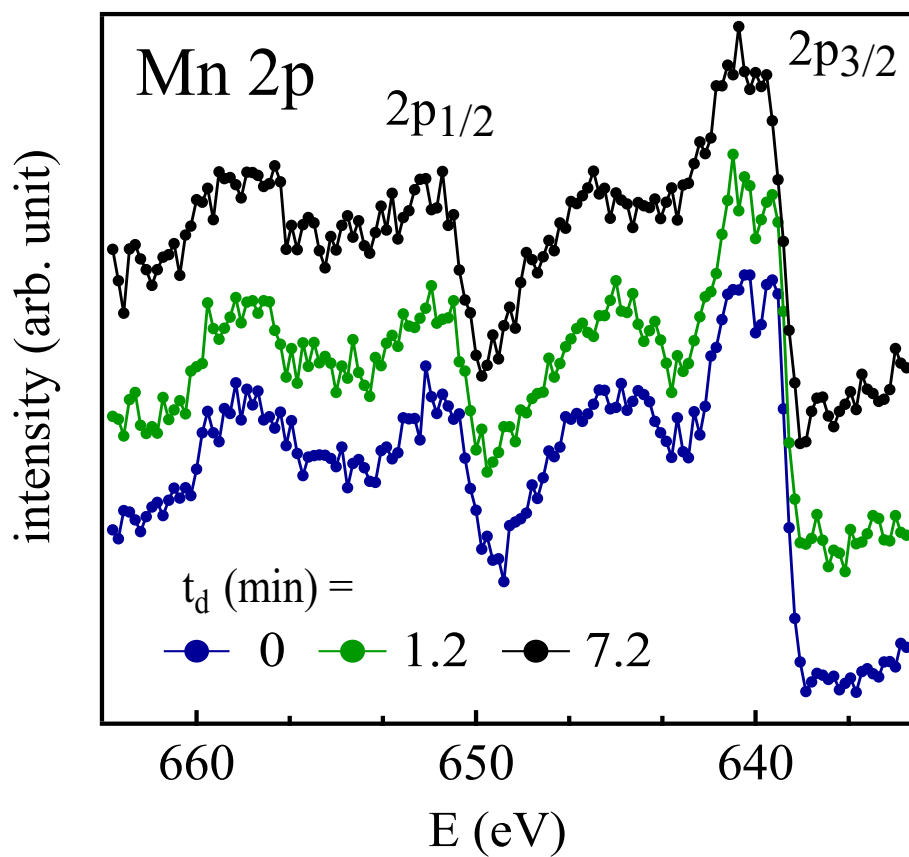


Fig. S 13. Mn 2p XPS core level spectra for different t_d compared to that of MBST. All the spectra are normalized to the same height.

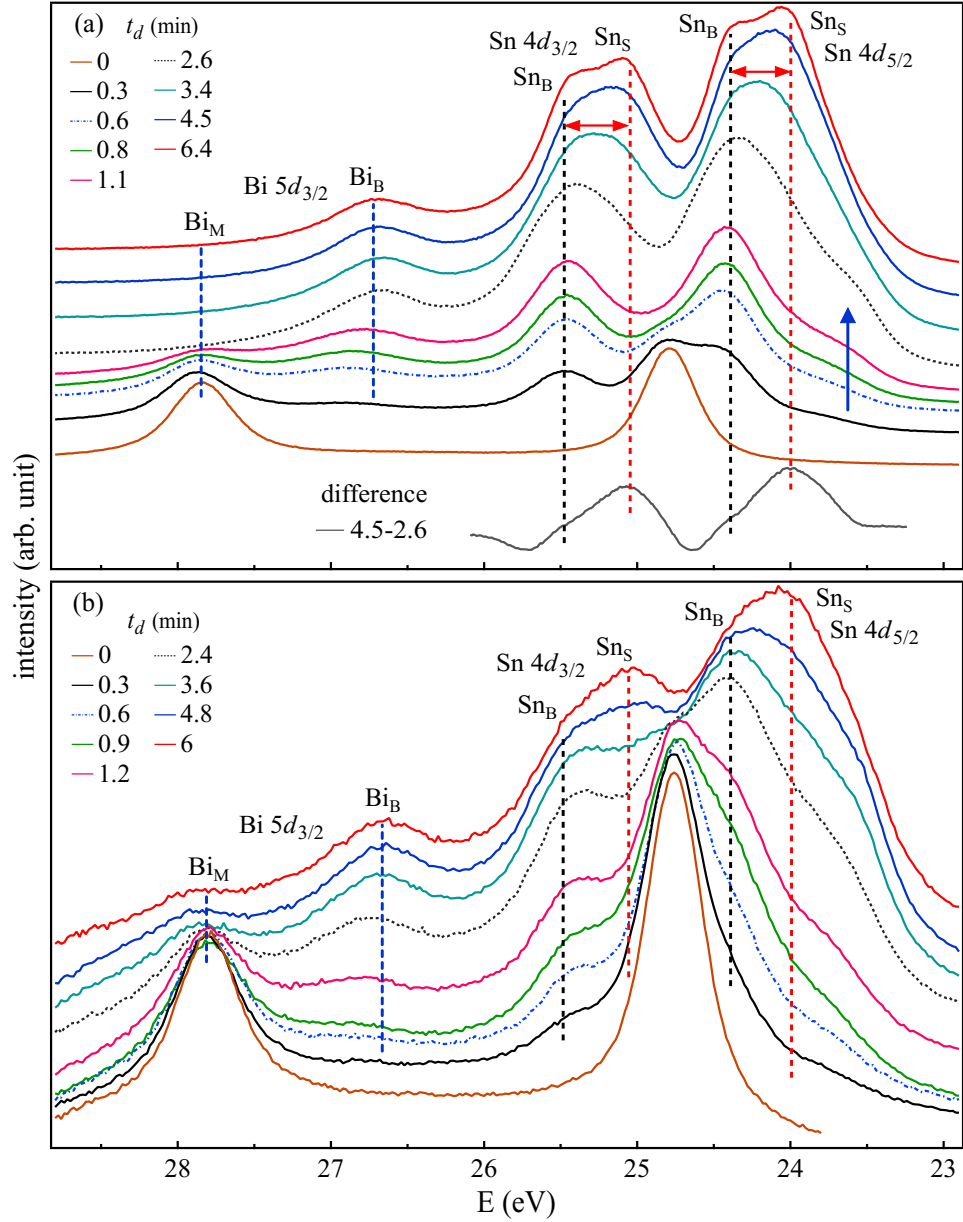


Fig. S 14. Sn 4d and Bi 5d shallow core level spectra taken with (a) 90 eV (synchrotron radiation) and (b) 40.8 eV (He II radiation) photon energies. t_d of the former is scaled with the latter. The stanene related Sn_S components (BL related Sn_B) for both the spin orbit components of Sn 4d are shown by red (black) dashed lines and also by the difference spectrum between primarily monolayer stanene ($t_d=4.5$ min) and BL ($t_d=2.6$ min). The Bi_B and Bi_M components of Bi $5d_{3/2}$ are shown by blue dashed lines (Bi_B component of Bi $5d_{5/2}$ is shown by blue arrow).

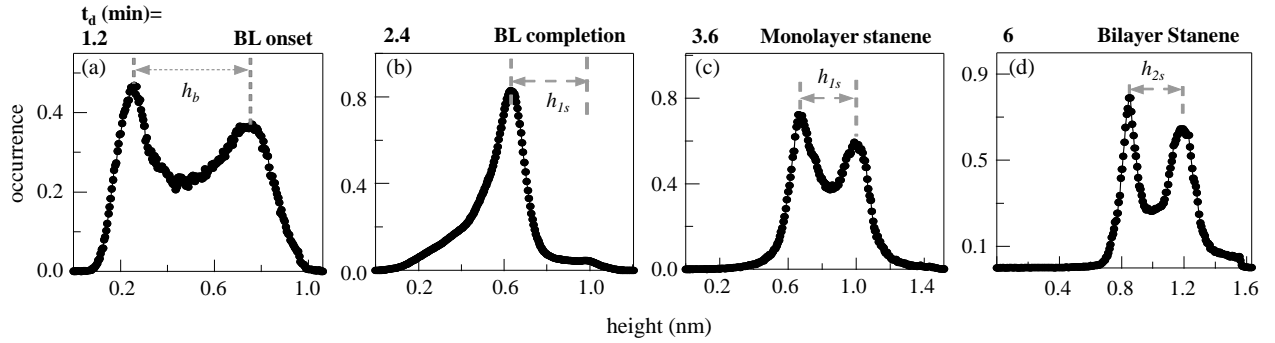


Fig. S 15. The height histograms corresponding to Figs. 3(a-d), respectively of the main manuscript. h_b , h_{1s} , h_{2s} represent the heights of the buffer layer, monolayer stanene and the bilayer stanene, respectively.

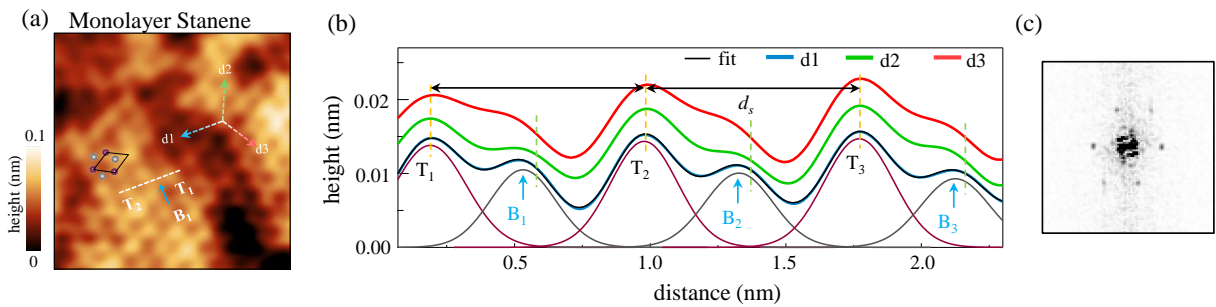


Fig. S 16. (a) An atomically resolved image of monolayer stanene region for $t_d = 3.6$ min ($4 \text{ nm} \times 4 \text{ nm}$, $I_T = 0.8 \text{ nA}$, $U_T = -0.75 \text{ V}$). (b) Average height profiles for panel a along d1, d2 and d3 directions, the former is fitted with Gaussian functions, symbols have same meaning as Fig. 3(j) of main manuscript. (c) The Fourier transform of panel a.

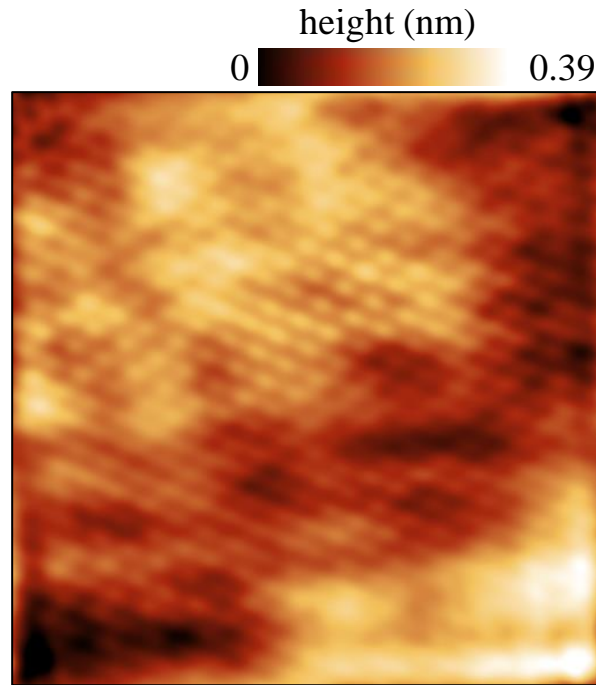


Fig. S 17. Atomic resolution STM topography of the BL for $t_d = 2.4$ min ($10 \text{ nm} \times 10 \text{ nm}$ with $I_T = 0.49$ nA and $U_T = -0.15$ V). The dark region in the lower left corner is the uncovered substrate.

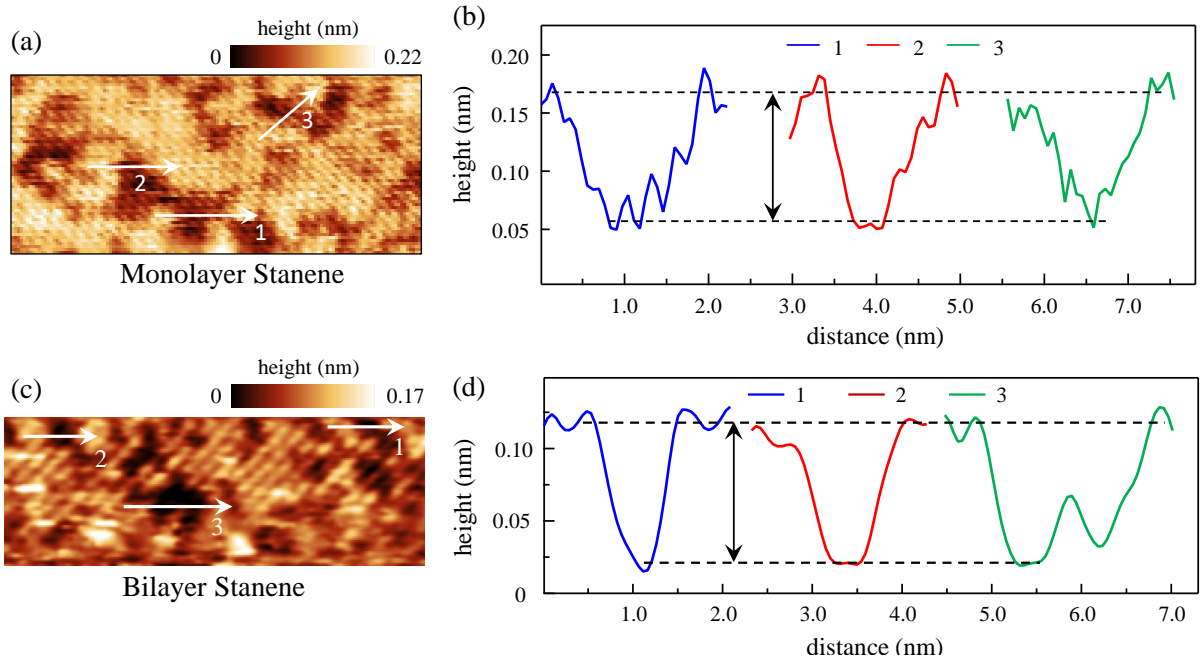


Fig. S 18. (a) STM topography ($9 \text{ nm} \times 4.3 \text{ nm}$, $I_T = 0.57 \text{ nA}$, and $U_T = 0.06 \text{ V}$) for monolayer stanene. (b) Height profiles across the upper and lower sublattice along the white arrows numbered 1-3 in panel a. (c) STM topography ($11 \text{ nm} \times 3.8 \text{ nm}$, $I_T = 0.45 \text{ nA}$, and $U_T = -0.7 \text{ V}$) for bilayer stanene. (d) Height profiles across the upper and lower sublattice along the white arrows numbered 1-3, as shown in panel c. The buckling height turns out to be $0.1 \pm 0.015 \text{ nm}$.

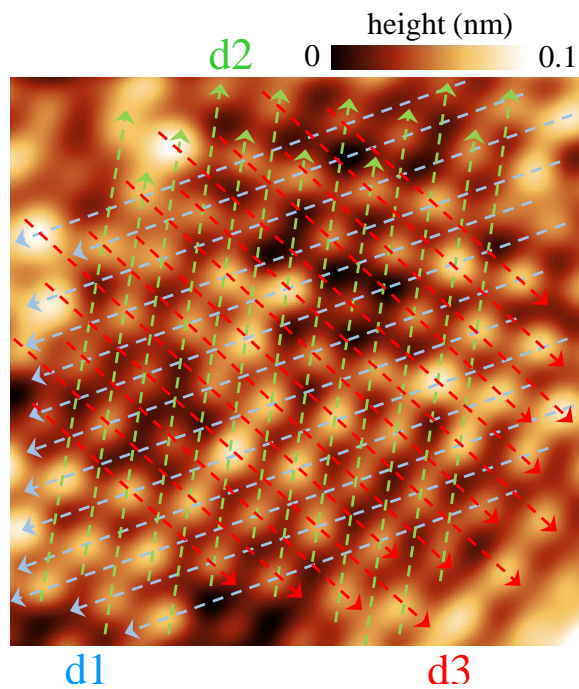


Fig. S 19. The atomic resolution STM image of bilayer stanene ($4 \text{ nm} \times 4 \text{ nm}$, same as Fig. 3(i) of main manuscript) shown overlaid by dashed blue, green and red lines along the d1, d2, and d3 directions, respectively along which the height profiles have been taken for averaging.

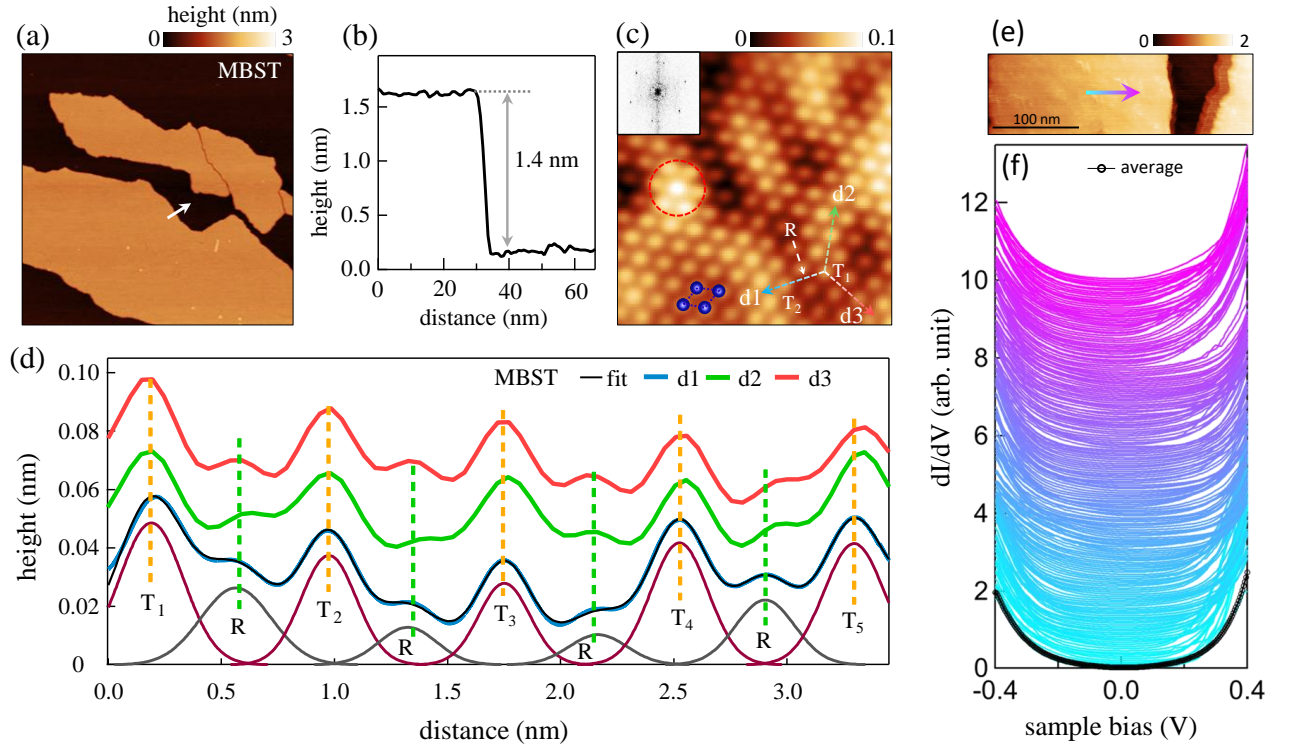


Fig. S 20. (a) Wide area STM topography ($400 \text{ nm} \times 400 \text{ nm}$ with tunneling current $I_T = 0.2 \text{ nA}$ and $U_T = -0.8 \text{ V}$) of the Te terminated MBST surface. (b) A height profile extracted along the white arrow shown in panel a quantifies the step height to be $1.4 \pm 0.03 \text{ nm}$, which is close to the 1.36 nm height of a single septuple layer of MBST shown in Fig. S3. (c) Atomic resolution STM image of the MBST surface ($5 \text{ nm} \times 5 \text{ nm}$ with $I_T = 0.7 \text{ nA}$ and $U_T = 0.4 \text{ V}$), inset shows the Fourier transform of this image. The unit cell is shown by blue dashed lines, blue circles represent Te atoms. A bright protrusion highlighted by a red dashed circle indicates presence of $(\text{Bi/Sb})_{\text{Te}}$ anti-site defect. (d) Height profiles from the atomic resolution image along the three different directions (d1, d2, d3), as shown in panel c. The profiles are fitted with Gaussian functions of nearly similar FWHM, fitting along d1 is shown by a black curve, where the peaks T_n , $n = 1-4$ (magenta curves) represent the atom positions and peaks indicated by R (gray curves) are attributed to the residual contribution that appears in the middle of $T_n T_{n+1}$. (e) STM topography image ($300 \text{ nm} \times 90 \text{ nm}$, $I_T = 0.1 \text{ nA}$ and $U_T = -0.4 \text{ V}$) of the MBST surface with an horizontal arrow of length of 73 nm along which dI/dV scanning tunneling spectra (STS) were taken at 201 equally separated points. (f) The waterfall plot of the STS spectra taken along the arrow in panel e, the black curve represents the average of all the spectra.

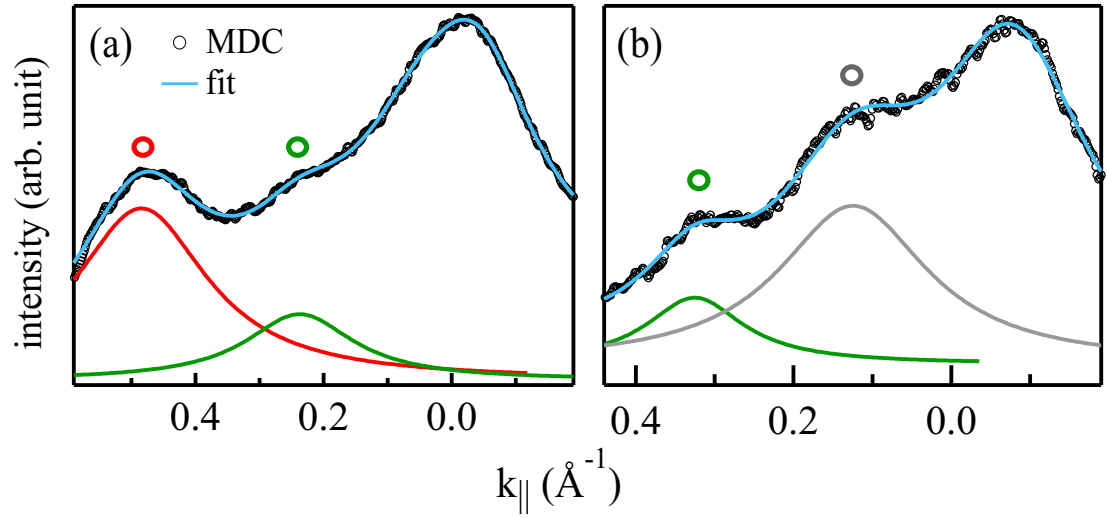


Fig. S 21. Curve fitting of the MDCs obtained from the raw ARPES intensity plot in Fig. 5(a) of the main manuscript shown for example at $E =$ (a) 0.25 eV and (b) 0.55 eV. The MDCs are fitted with Lorentzian functions, the fitted curve is shown in cyan color. In panel **a** red (green) open circle and the maximum of the curve represents the peak position of outer (inner) hole band. In panel **b**, green (gray) open circle and the maximum of the curve represents the peak position of the inner hole (inverted parabolic) band.

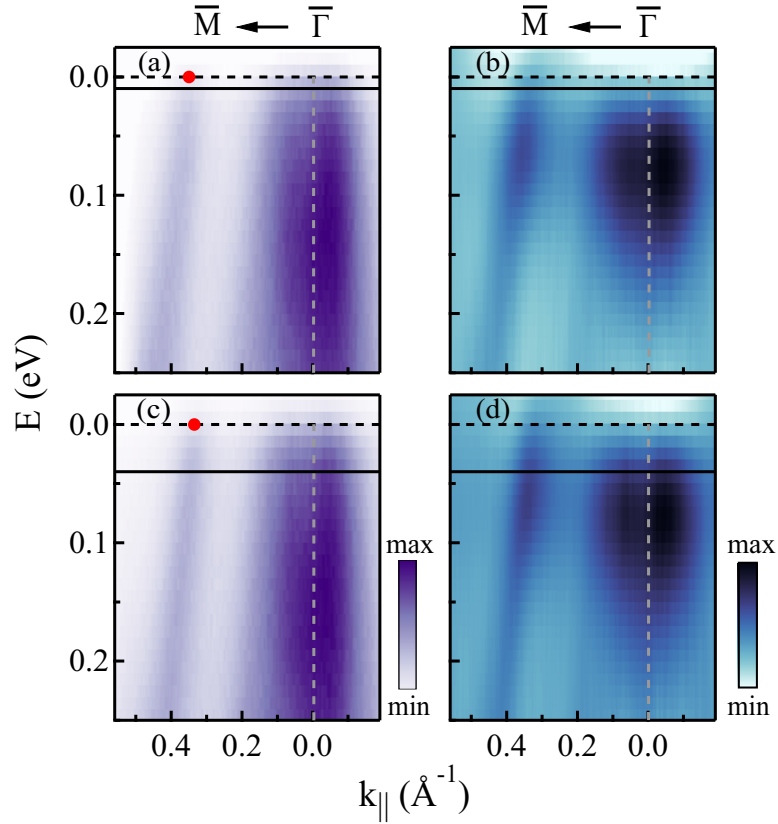


Fig. S 22. ARPES intensity plot and its second derivative plot after (a, b) 10 sec and (c, d) 30 sec potassium deposition on stanene, respectively. Red circles in panels **a** and **c** indicate the position of the outer hole band at E_F obtained from fitting the MDC. The black solid line is the E_F position before K deposition.

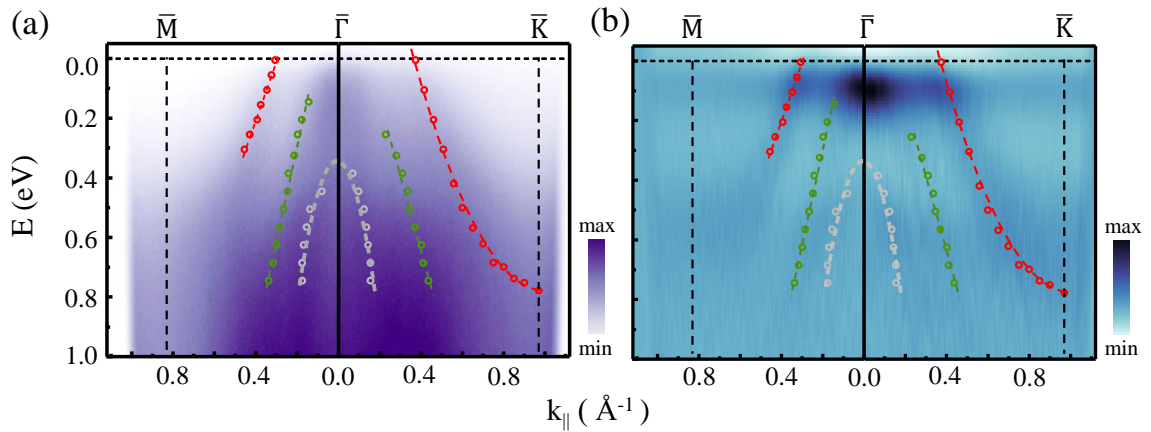


Fig. S 23. (a) Raw and (b) second derivative intensity plots towards the $\bar{M}\text{-}\bar{\Gamma}\text{-}\bar{K}$ direction up to \bar{M} and \bar{K} points. This intensity plot was measured at room temperature and has slightly inferior statistics in comparison to the data in Fig. The bands obtained from Fig. 5 are superimposed.

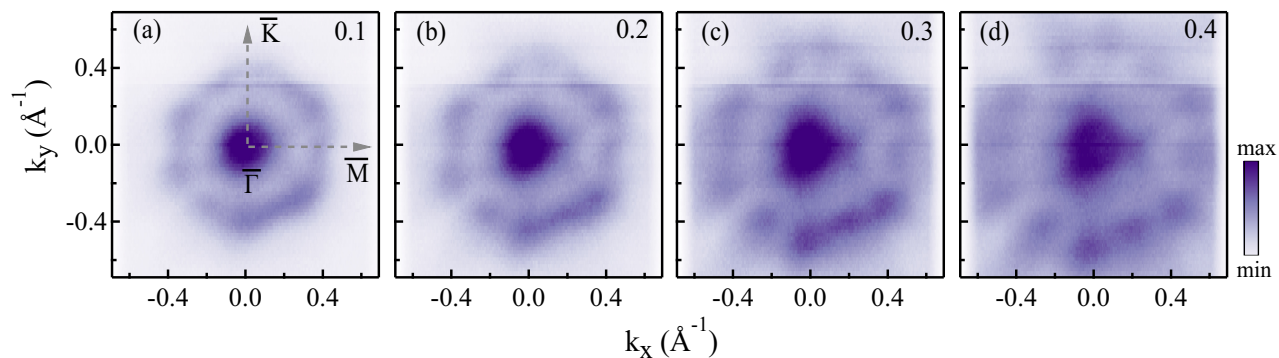


Fig. S 24. (a-d) k_x - k_y isosurface plots for E varying from 0.1 to 0.4 eV, as shown in the upper right corner of each panel. The segmentation in the isosurface plot with lower intensity in between \bar{K} and \bar{M} points could be related to characteristic dispersion of the outer band. These plots are obtained by averaging over ± 15 meV for each E .

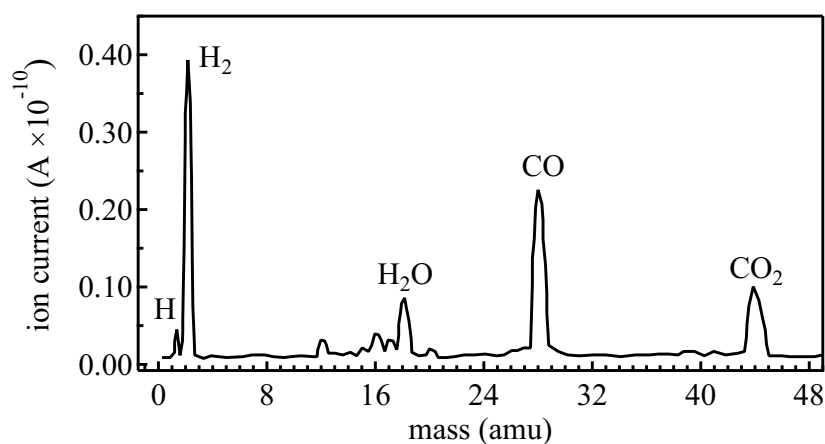


Fig. S 25. A residual mass spectrum recorded with a quadrupole mass spectrometer mounted on the preparation chamber where stanene was grown. The origin of the various dominant peaks is indicated, demonstrating that hydrogen is the most prevalent residual gas.

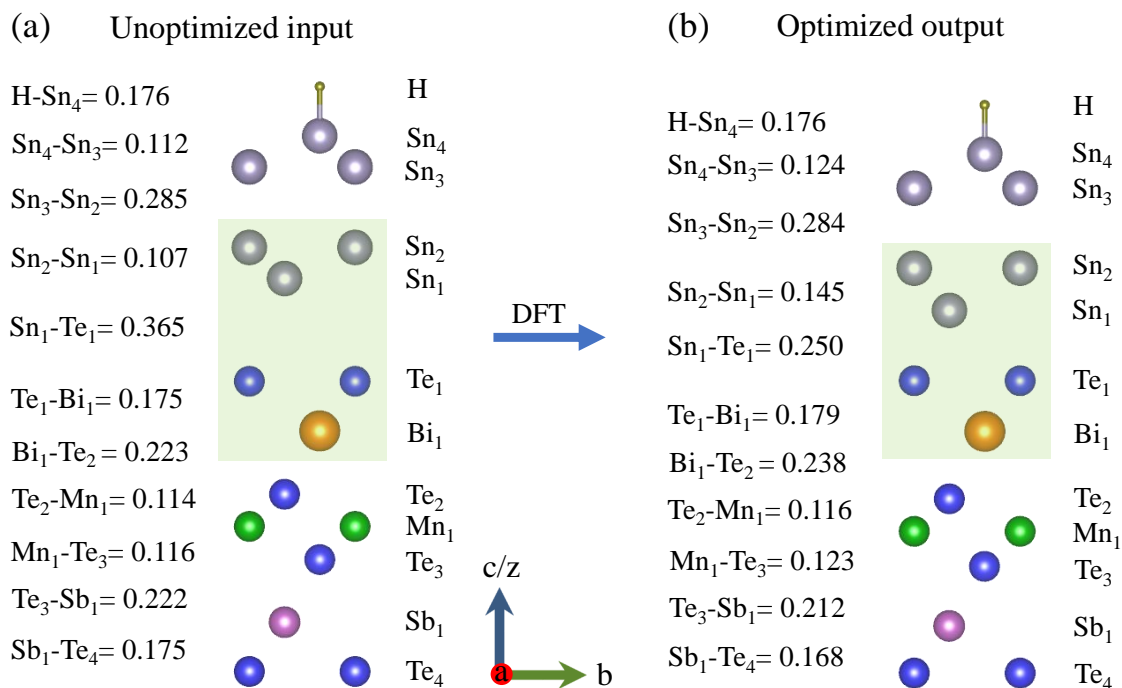


Fig. S 26. (a) The unoptimized input structure and (b) the optimized output structure of “S+BL+H” DFT calculation for monolayer stanene on MBST including BL (green shading) and H passivation (topmost layer). The labeled atoms are represented by size-scaled circles of various colors, as in Fig. 5(h) of the main manuscript. Both the structures have been drawn in the same scale using the VESTA program [2]. The separations between the adjacent layers are indicated for both the structures in nm.

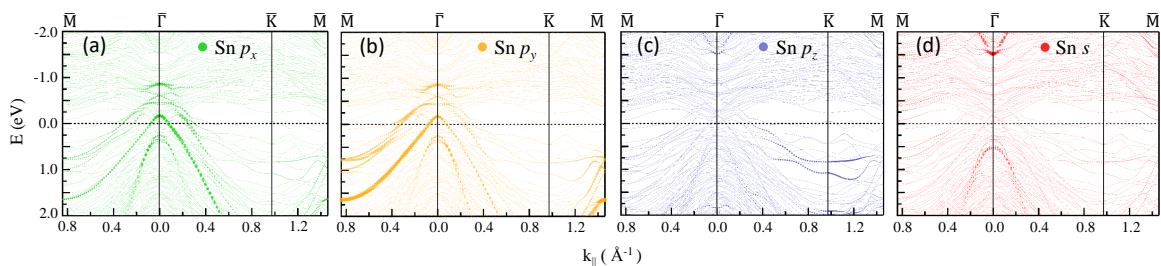


Fig. S 27. The Sn (a) p_x , (b) p_y , (c) p_z , and (d) s orbital character of the bands for the “S+BL+H” DFT calculation for monolayer stanene on MBST including BL and H passivation.

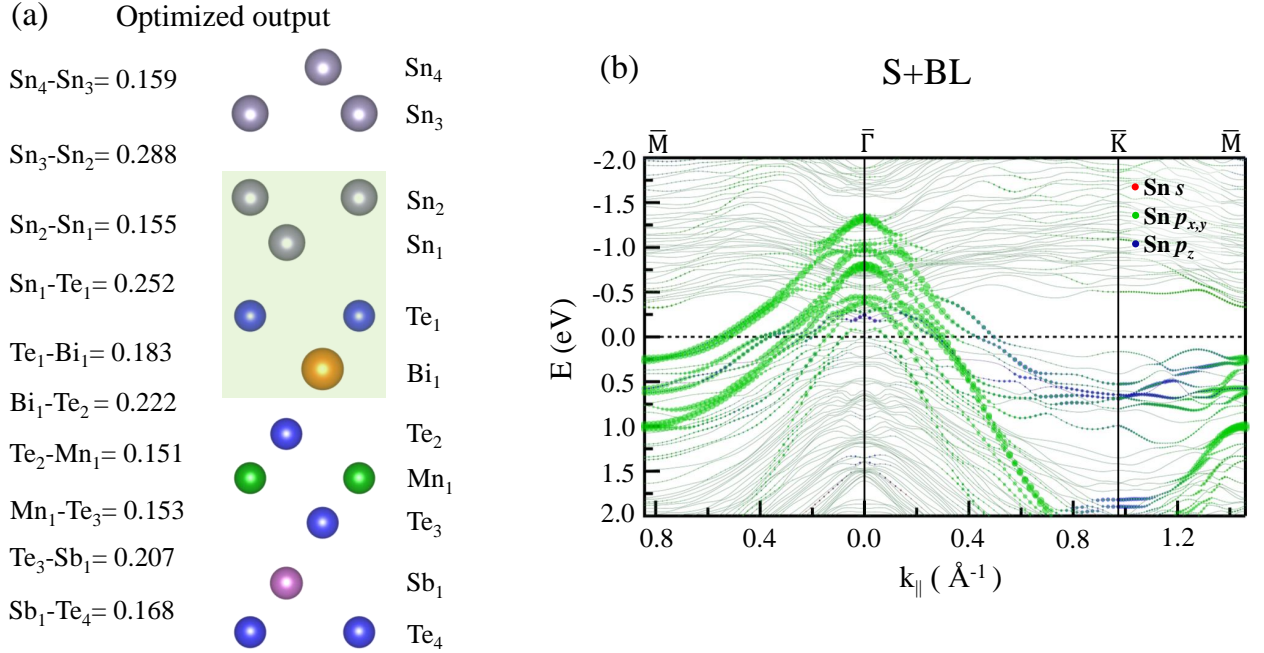


Fig. S 28. (a) The optimized output structure of “S+BL” DFT calculation for monolayer stanene on MBST including a BL (green shading) but without H passivation. The labeled atoms are represented by size-scaled circles of various colors, as in Fig. 5(h) of the main manuscript. The separations between the adjacent layers are indicated in nm. (b) The calculated band dispersion including SOC for “S+BL” along $\overline{M}\text{-}\overline{\Gamma}\text{-}\overline{K}\text{-}\overline{M}$ directions. The bands of Sn $p_{x,y}$, p_z , and s character are highlighted.

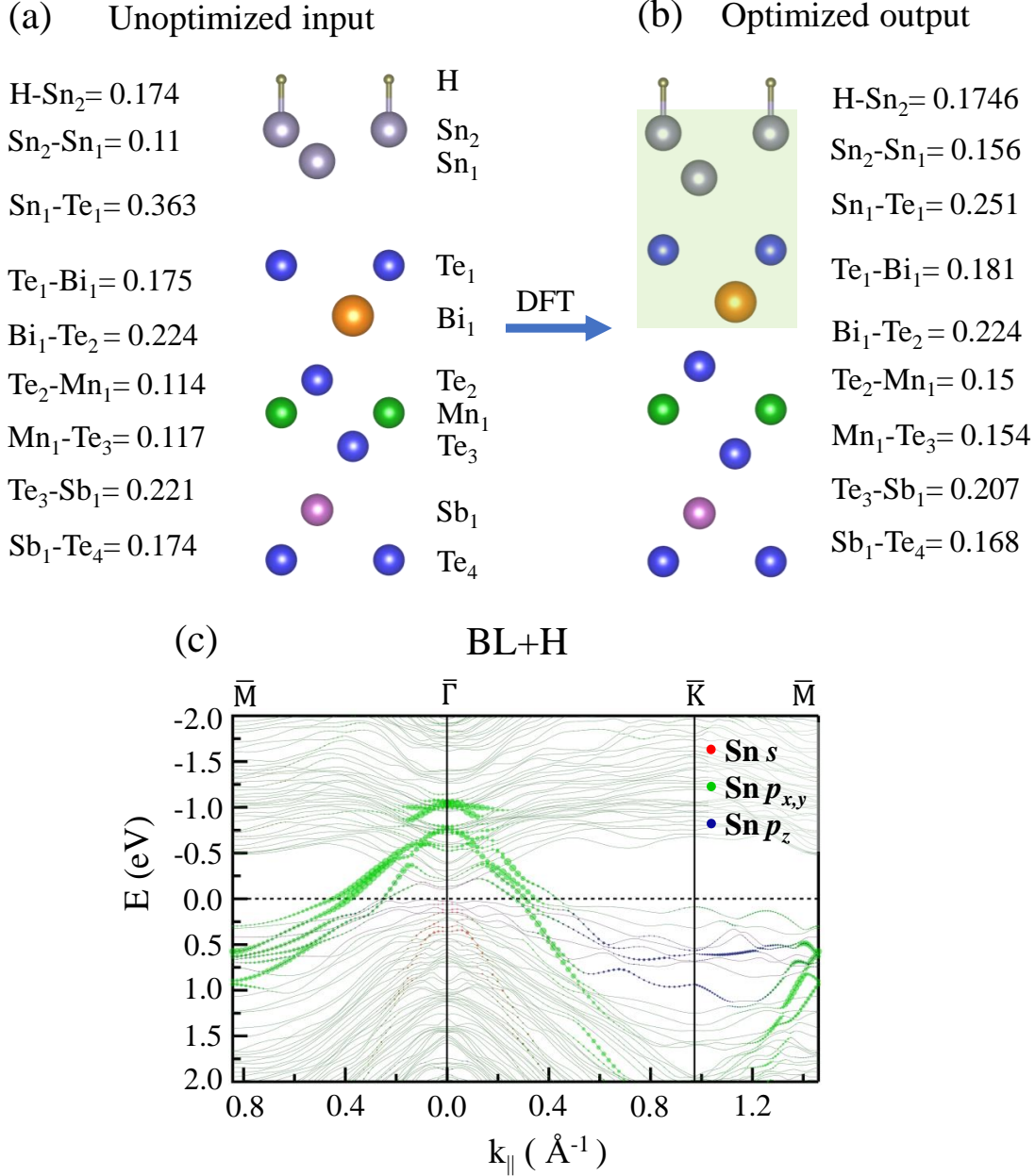


Fig. S 29. (a) The unoptimized input structure and (b) the optimized output structure of “BL+H” DFT calculation for BL (green shading) on MBST including H passivation (topmost layer). Both the structures have been drawn in the same scale using the VESTA program [2]. The labeled atoms are represented by size-scaled circles of various colors, as in Fig. 5(h) of the main manuscript. The separations (in nm) between the adjacent layers are indicated for both panels, **a** and **b**. (c) The calculated band dispersion including SOC for “BL+H” along \bar{M} - $\bar{\Gamma}$ - \bar{K} - \bar{M} directions. The bands of Sn $p_{x,y}$, p_z , and s character are highlighted.

-
- [1] J.-Q. Yan, S. Okamoto, M. A. McGuire, A. F. May, R. J. McQueeney, and B. C. Sales, *Evolution of structural, magnetic, and transport properties in $MnBi_{2-x}Sb_xTe_4$* , Phys. Rev. B **100**, 104409 (2019).
- [2] K. Momma and F. Izumi, *VESTA 3 for three-dimensional visualization of crystal, volumetric and morphology data*, J. Appl. Crystallogr. **44**, 1272 (2011).